Aluminum 2024-T351 Input Parameters for *MAT_224 in LS-DYNA

Part 3: Ballistic Impact Simulations of an Aluminum 2024 Panel Using *MAT_224 in LS-DYNA Considering Oblique Incidence and Attitude Angles of a Rectangular Projectile

May 2020

Final Report

U.S. Department of Transportation
Federal Aviation Administration

NOTICE

This document is disseminated under the sponsorship of the U.S. Department of Transportation in the interest of information exchange. The U.S. Government assumes no liability for the contents or use thereof. The U.S. Government does not endorse products or manufacturers. Trade or manufacturers' names appear herein solely because they are considered essential to the objective of this report. The findings and conclusions in this report are those of the author(s) and do not necessarily represent the views of the funding agency. This document does not constitute FAA policy. Consult the FAA sponsoring organization listed on the Technical Documentation page as to its use.

This report is available at the Federal Aviation Administration William J. Hughes Technical Center's Full-Text Technical Reports page: actlibrary.tc.faa.gov in Adobe Acrobat portable document format (PDF).

1. Report No. DOT/FAA/TC-19/41, P3	2. Government Accession No.	3. Recipient's Catalog No.
4. Title and Subtitle Aluminum 2024-T351 Input Parameters for *MAT_224 in LS-DYNA, Part 3: Ballistic Impact Simulations of an Aluminum 2024 Panel Using *MAT_224 in LS-DYNA Considering Oblique Incidence and Attitude Angles of a Rectangular Projectile		5. Report Date May 2020
		6. Performing Organization Code
7. Author(s) Chung-Kyu Park[1], Gilbert Queitzsch (retired)[2], Kelly Carney[1], Paul Du Bois[1], Cing-Dao Kan[1], Daniel Cordasco[3], and William Emmerling[3]		8. Performing Organization Report No.
9. Performing Organization Name and Address [1] George Mason University, Center for Collision Safety and Analysis 4087 University Drive, Fairfax, VA 22030 USA [2] Federal Aviation Administration 950 L'Enfant Plaza North, S.W., Washington, DC 20024 [3] Federal Aviation Administration, William J. Hughes Technical Center Atlantic City International Airport, NJ 08405		10. Work Unit No. (TRAIS)
		11. Contract or Grant No. 692M151840003
12. Sponsoring Agency Name and Address U.S. Department of Transportation Federal Aviation Administration Air Traffic Organization Operations Planning Office of Aviation Research and Development Washington, DC 20591		13. Type of Report and Period Covered Final Report
		14. Sponsoring Agency Code AIR-6A1

15. Supplementary Notes

The Federal Aviation Administration William J. Hughes Technical Center Aviation Research Division Technical Monitor was Daniel Cordasco.

16. Abstract

The material dataset of *MAT_224 in LS-DYNA for Aluminum 2024 (Version 2.0) was recently updated and validated to improve the numerical modeling of turbine engine blade-out containment tests and assess uncontained threats to aircraft structures. Both of these assessments are required for certification of civil aircraft and aircraft engines. This newly updated numerical material model for Aluminum 2024 was utilized to conduct the simulations of additional NASA ballistic impact tests. The objectives of this study are (1) to validate the new material model with complex impact conditions; (2) to evaluate the predictability of ballistic limit and residual velocities of a projectile under various impact conditions; and (3) to investigate the effects of oblique incidence and attitude angle variations of a rectangular projectile on penetration of a target plate.

NASA conducted the additional series of ballistic impact tests that provided experimental data to evaluate the numerical material model for Aluminum 2024 using *MAT_224 under more extreme conditions than had been evaluated previously with spherical or cylindrical projectiles impacting at normal incidence. In the test program, a rectangular, parallelepiped projectile was selected because it provided sharp corner-and-edge contact geometries when impacting flat panels at oblique angles of incidence. The projectiles were fabricated from Inconel 718 and the flat plates from Aluminum 2024. Test impact velocities ranged from approximately 140 fps to 350 fps. Impact locations were at the plate center and off-center. Projectile oblique impact angles were 0°, 30°, and 45°, and roll angles were 0°, 30°, 60°, and 90°. Based on the combination of desired impact orientations and velocities, 11 test setups were considered; 34 impact tests were conducted.

A full ballistic impact simulation model for the projectile and target plate was created using over 20 million solid elements to conduct approximately 100 ballistic impact simulations. Overall, the ballistic impact simulations showed highly comparable results with the NASA tests in terms of projectile residual velocities, failure shapes of the target plates, and projectile penetration behavior. Based on a series of ballistic impact simulations, the ballistic limit velocities of the projectile were predicted using the method of least squares, which showed a good correlation with the NASA tests. These results demonstrate that the updated Aluminum 2024 *MAT_224 parameters produces a truly predictive material model. In addition, the effects of oblique angle change of the projectile were investigated, and the sensitivity of the attitude angle variation was studied.

17. Key Words ballistic impact simulation, aluminum 2024, oblique angle, attitude angle, *MAT_224, LS-DYNA	18. Distribution Statement This document is available to the U.S. public through the National Technical Information Service (NTIS), Springfield, Virginia 22161. This document is also available from the Federal Aviation Administration William J. Hughes Technical Center at actlibrary.tc.faa.gov.		
19. Security Classif. (of this report) Unclassified	20. Security Classif. (of this page) Unclassified	21. No. of Pages	22. Price

Form DOT F 1700.7 (8-72)   Reproduction of completed page authorized

ACKNOWLEDGEMENTS

TABLE OF CONTENTS

LIST OF FIGURES

LIST OF TABLES

LIST OF ACRONYMS

ACFPP	Aircraft Catastrophic Failure Prevention Program
CCSA	Center for Collision Safety and Analysis
CG	Center of Gravity
FE	Finite Element
GMU	George Mason University
GRC	Glenn Research Center
GWU	George Washington University
HPC	High Performance Computing
NASA	National Aeronautics and Space Administration
OSU	Ohio State University
RMS	Root Mean Square

EXECUTIVE SUMMARY

The material dataset of *MAT_224 in LS-DYNA for Aluminum 2024 (Version 2.0) was recently updated and validated to improve the numerical modeling of turbine engine blade-out containment tests and assess uncontained threats to aircraft structures. Both of these assessments are required for certification of civil aircraft and aircraft engines. This newly updated numerical material model for Aluminum 2024 was utilized to conduct the simulations of additional NASA ballistic impact tests. The objectives of this study are: (1) to validate the new material model with complex impact conditions; (2) to evaluate the predictability of ballistic limit and residual velocities of a projectile under various impact conditions; and (3) to investigate the effects of oblique incidence and attitude angle variations of a rectangular projectile on penetration of a target plate.

NASA conducted the additional series of ballistic impact tests that provided experimental data to evaluate the numerical material model for Aluminum 2024, using *MAT_224 under more extreme conditions than previously evaluated with spherical or cylindrical projectiles impacting at normal incidence. In the test program, a rectangular, parallelepiped projectile was selected because it provided sharp corner-and-edge contact geometries when impacting flat panels at oblique angles of incidence. The projectiles were fabricated from Inconel 718, and the flat plates from Aluminum 2024. Test impact velocities ranged from approximately 140 fps to 350 fps. Impact locations were at the plate center and off-center. Projectile oblique impact angles were 0º, 30º, and 45º; roll angles were 0º, 30º, 60º, and 90º. Based on the combination of desired impact orientations and velocities, 11 test setups were considered; 34 impact tests were conducted.

A full ballistic impact simulation model for the projectile and target plate was created using over 20 million solid elements to conduct approximately 100 ballistic impact simulations. Overall, the ballistic impact simulations showed highly comparable results with the NASA tests in terms of projectile residual velocities, failure shapes of the target plates, and projectile penetration behavior. Based on a series of ballistic impact simulations, the ballistic limit velocities of the projectile were predicted using the method of least squares, which showed a good correlation with the NASA tests. These results demonstrate that the updated Aluminum 2024 *MAT_224 parameters produce a truly predictive material model. In addition, the effects of oblique angle change of the projectile were investigated, and the sensitivity of the attitude angle variation was studied.

1. INTRODUCTION

A team consisting of George Mason University (GMU), Ohio State University (OSU), George Washington University (GWU), the National Aeronautics and Space Administration (NASA) - Glenn Research Center (GRC), and the Federal Aviation Administration (FAA) - Aircraft Catastrophic Failure Prevention Program (ACFPP) collaborated to develop a new material model in LS-DYNA for metallic materials. The research was directed towards improving the numerical modeling of turbine engine blade-out containment tests required for certification of aircraft engines [1]. In this effort, the LS-DYNA constitutive material model *MAT_TABULATED_ JOHNSON_COOK, or simply *MAT_224, was previously developed and subsequently updated [2, 3]. *MAT_224 is a general elasto-visco-plastic material model that incorporates arbitrary stress versus strain curves to define material plasticity, including arbitrary strain rate and temperature dependency. The element erosion criterion is the plastic failure strain, which can be defined as a function of the state of stress, strain rate, temperature and element size.

The original *MAT_224 input parameters (Version 1.3) for Aluminum 2024-T351 alloy were developed [2] based on tabulated data from several material tests performed by OSU [2, 4]. However, the original model did not produce simulations that accurately matched the ballistic impact tests for the range of conditions desired [5]. In addition, continuing research to develop material models for Titanium 6Al-4V and Inconel 718 alloys revealed deficiencies in the original Aluminum mechanical test data. Improved measurement techniques in material tests have since been developed, along with new test methods that provide additional model calibration points on the failure surface. Based on this later work, the updated *MAT_224 input parameters (Version 2.0) for Aluminum 2024-T351 alloy were developed and released recently [6]. In the development process, additional material tests were conducted, and improved test measurement techniques were adopted. The updated material model was validated by the series of ballistic impact tests using spherical and cylindrical projectiles normal to Aluminum 2024 panels of various thicknesses. Overall, the ballistic impact simulations using the updated material model show better correlation to the tests for a broader range of test conditions.

NASA conducted a series of ballistic impact tests to provide experimental data to evaluate the numerical material model under more extreme conditions, using a rectangular parallelepiped shaped projectile with sharp corners and edges (45° edge chamfer to minimize handling damage and reduce numerical sensitivity), impacting flat panels at oblique angles of incidence [7]. In the tests, a hardened rectangular block of Inconel 718 impacts an Aluminum 2024 flat panel with various impact velocities (140 fps ~ 350 fps), impact locations (center and off-center), oblique impact angles (0°, 30°, and 45°), and projectile roll angles (0°, 30°, 60°, and 90°). Based on the combination of various impact conditions, 11 test setups were considered, and 34 impact tests were conducted.

The range of the test velocities selected resulted in impacts that were sensitive to material properties and projectile shapes and orientations. These test velocities are typical for those observed in uncontained turbine engine blade failures. These test velocities also result in complex failure modes, unlike at higher velocities, which are primarily shear failure.

The objectives of this study are: (1) to validate the new material model with complex impact conditions; (2) to evaluate the predictability of ballistic limit and residual velocities of a projectile under various impact conditions; and (3) to investigate the effects of oblique and attitude angle variations of the rectangular projectile on penetration of the target plate. The newly developed *MAT_224 for Aluminum 2024 was utilized to conduct a series of ballistic impact simulations of the NASA tests. As a result, over 100 ballistic impact simulations were conducted, and their results analyzed.

2. DESCRIPTION OF THE BALLISTIC IMPACT CONFIGURATION

Figure 1 illustrates the rectangular projectile geometry. The rectangular block is hollow with three channels running lengthwise in the long direction of the block. The hollow passages are included to achieve a desired density relevant to a range of potential engine debris fragments. The block has three different area faces (front, side, and top) and three different length edges (short, mid, and long). The projectile local coordinate system (x_p, y_p and z_p) is defined with its origin at the center of gravity (CG) of the projectile and x-, y-, and z-axis oriented as shown.
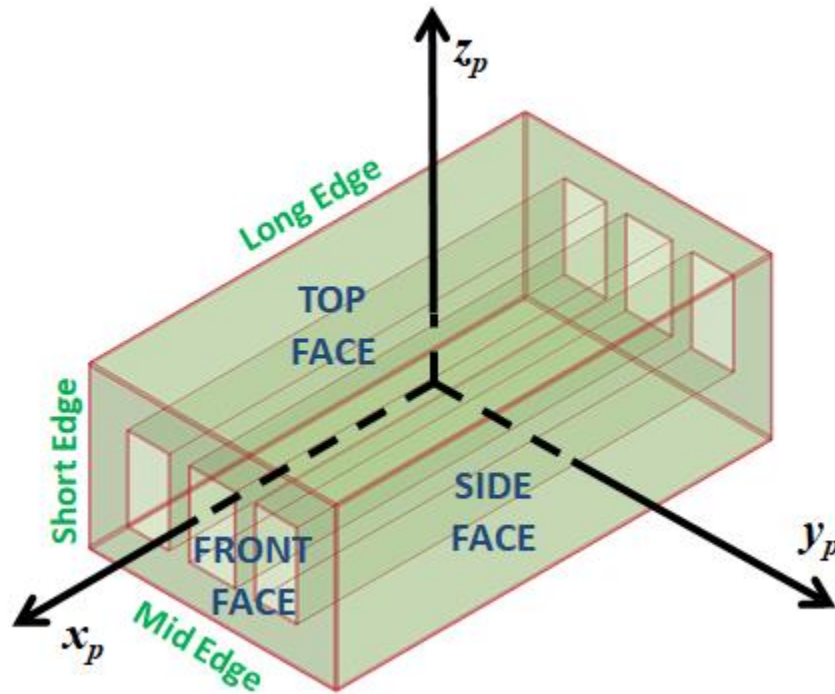
Figure 1. Rectangular projectile geometry

Figure 2 depicts the ballistic impact of the rectangular projectile against the flat target plate. There are three different coordinate systems: the global coordinate system (X, Y, and Z), projectile local coordinate system (x_p, y_p, and z_p), and target plate local coordinate system (x_t, y_t, and z_t). The projectile is fired with its CG traveling along the global X-axis. The target plate local coordinate

system is located at the cross-point where the projectile CG flight direction ($\vec{b}$) intersects the impact surface of the target plate. The origin of the target plate local coordinate system is located on the X-axis of the global coordinate system. The projectile flight direction ($\vec{b}$) is parallel to the X-axis of the global coordinate system. The attitude angle is the orientation of the projectile relative to the projectile flight path and is described by the Euler angles (roll, pitch, and yaw) of the projectile. The oblique angle (α) is defined as the angular orientation between the normal ($\vec{n'}$) of the target plate and the flight direction ($\vec{b}$) of the projectile. Principally, there are three impact configurations—face, edge, and corner impacts—based on the initial contact geometry of the projectile against the target plate.
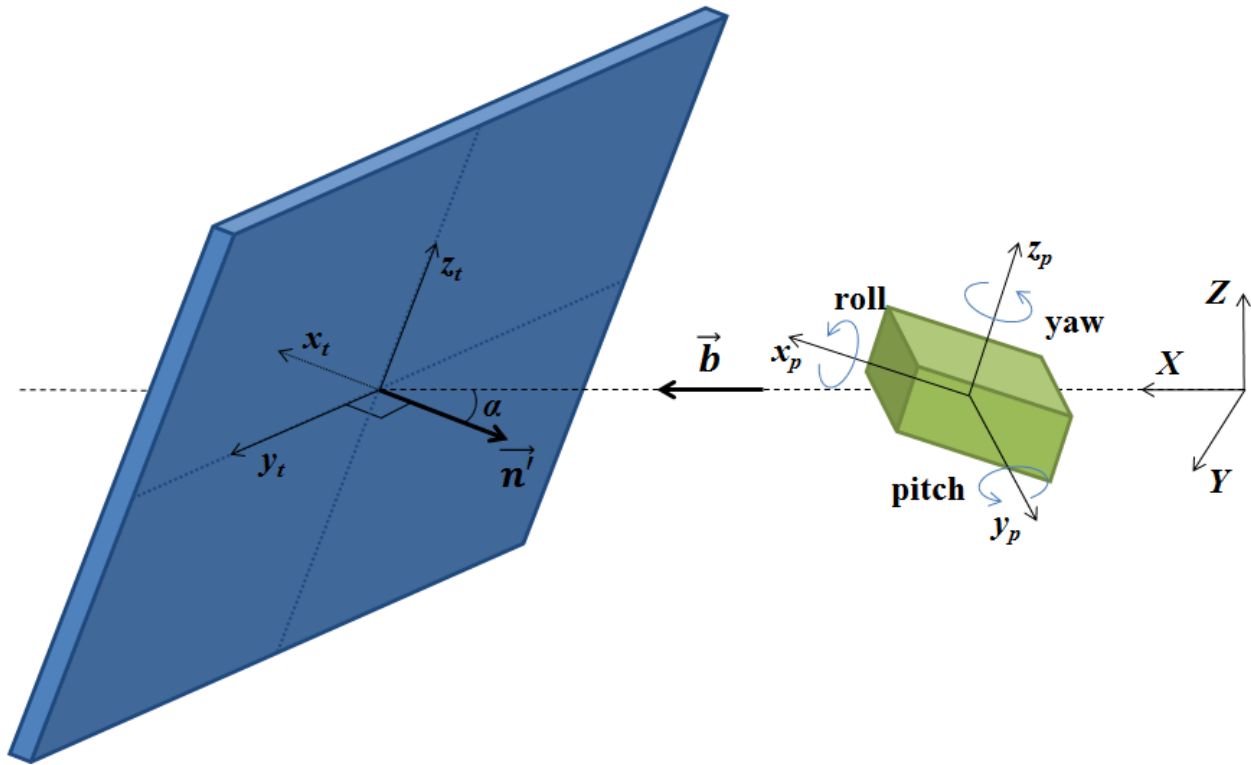
Figure 2. Depiction of the ballistic impact of the rectangular projectile against the flat plate

The original normal ($\vec{n}$) of the target plate, which is initially parallel to the X-axis of the global coordinate system, and the flight direction ($\vec{b}$) of the projectile in the global coordinate system are defined as

$$\vec{n} = (-1 \quad 0 \quad 0)^T \text{ and} \tag{2.1}$$

$$\vec{b} = (1 \quad 0 \quad 0)^T . \tag{2.2}$$

Considering the intrinsic rotation of the target plate in the target plate local coordinate system, the rotation matrix of the rotation (ϕ, θ, ψ) of the target plate in the Z-Y-X sequence is defined as

$$\widehat{\boldsymbol{R}}_t(\phi, \theta, \psi) = \widehat{\boldsymbol{R}}_{z_t}(\phi) \cdot \widehat{\boldsymbol{R}}_{y_t}(\theta) \cdot \widehat{\boldsymbol{R}}_{x_t}(\psi) \ . \tag{2.3}$$

where,

$$\widehat{\boldsymbol{R}}_{z_t}(\psi) = \begin{pmatrix} cos\psi & -sin\psi & 0 \\ sin\psi & cos\psi & 0 \\ 0 & 0 & 1 \end{pmatrix}. \tag{2.4}$$

$$\widehat{\boldsymbol{R}}_{y_t}(\theta) = \begin{pmatrix} cos\theta & 0 & sin\theta \\ 0 & 1 & 0 \\ -sin\theta & 0 & cos\theta \end{pmatrix}, \text{ and} \tag{2.5}$$

$$\widehat{\boldsymbol{R}}_{x_t}(\phi) = \begin{pmatrix} 1 & 0 & 0 \\ 0 & cos\phi & -sin\phi \\ 0 & sin\phi & cos\phi \end{pmatrix}, \tag{2.6}$$

Then, the updated normal $(\overrightarrow{\boldsymbol{n'}})$ of the rotated target plate is obtained as

$$\overrightarrow{\boldsymbol{n'}} = \widehat{\boldsymbol{R}}_t(\phi, \theta, \psi) \cdot \overrightarrow{\boldsymbol{n}} \tag{2.7}$$

Finally, the oblique angle (α) between the normal $(\overrightarrow{\boldsymbol{n'}})$ of the target plate and the flight direction $(\overrightarrow{\boldsymbol{b}})$ of the projectile is obtained from

$$\alpha = cos^{-1} \left| \frac{\overrightarrow{\boldsymbol{b}} \cdot \overrightarrow{\boldsymbol{n'}}}{|\overrightarrow{\boldsymbol{b}}| \cdot |\overrightarrow{\boldsymbol{n'}}|} \right| \ . \tag{2.8}$$

3. NASA BALLISTIC IMPACT TEST

NASA conducted a series of ballistic impact tests to provide experimental data to evaluate the numerical material model under more extreme conditions, using a projectile with a more complex shape and sharp contacts, impacting flat panels at oblique angles of incidence [7]. This section briefly introduces the NASA ballistic impact tests.

Figure 3(a) shows the hollow, rectangular, parallelepiped-shaped projectile with sharp corners and edges designed for the NASA ballistic tests. It has 45° chamfers with approximately 0.01" cutting edge height to minimize handling damage and reduce sensitivity in the corresponding finite element model. The nominal dimensions of the projectile are 55.88 mm (2.2 in.) long by 31.75 mm (1.25 in.) high by 20.83 mm (0.82 in.) wide. The projectile was manufactured from Inconel 718 and heat-treated to a hardness of 44 Rockwell C. Three rectangular channels were machined through the center of the projectile in the long direction to reduce the overall mass and effective density. The mass of the projectiles ranged from 220.45 gm to 222.45 gm, with an average mass of 221.52 gm. High-speed photography made use of the white dots on the projectile to capture projectile orientation (pitch, yaw, and roll) along the flight path during each test.

4
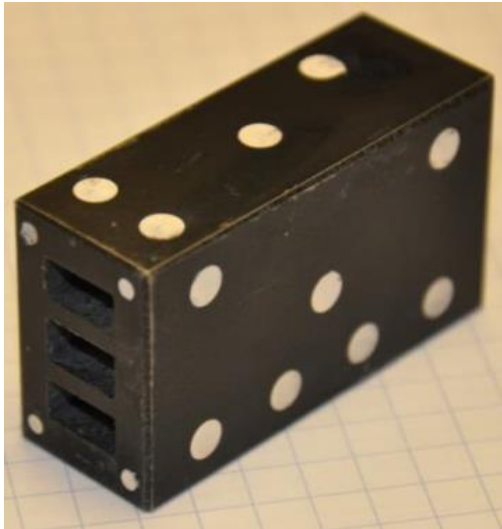
(a)   (b)

Figure 3. Projectile and panel [7]: (a) projectile and (b) panel

Figure 3(b) shows the typical rectangular impact test panel. The nominal dimensions of the panel are 30.48 cm (12 in.) wide by 53.34 cm (21 in.) long, and 3.20 mm (0.126 in.) thick. The panel material is Aluminum 2024-T3. The panels were sandwiched between 12.7 mm (0.5 in.) thick front and back frames with an aperture of 22.86 cm (9 in.) wide by 45.72 cm (18 in.) tall. The front frame has outer dimensions the same as the test panel. The panels were attached by 28 through bolts connecting the front frame, panel, and back frame.

In the ballistic impact tests, the rectangular projectile impacts the Aluminum 2024 flat panel under various impact conditions (projectile velocity and orientation) and four impact settings (varying locations on the target and target orientations).

- The two impact locations are at the center and at the off-center quarter point of the panel. The off-center impact point is located at three-fourths of the distance from the bottom of the test panel to the top along the centerline of the panel width for all the off-center impact location cases.
- The three target panel tilt angles are 0º, 30º, and 45º. (The target tilt was used to set the oblique angle.)

- The four projectile roll angles are 0º, 30º, 60º, and 90º. (The projectile roll is used to set the edge/corner orientation relative to the target. The roll is the only component of attitude that had to be varied to accomplish the different face, edge, and corner impacts desired.)
- The impact velocity of the projectile was varied from 140 fps to 350 fps to identify the ballistic limit velocity.

Based on the combination of different impact settings, 11 test setup cases were considered, with 34 impact tests conducted. Table 1 summarizes these setup cases. Figure 4 shows one test setup where the target/support frame is depicted in exploded view for clarity. In this NASA test series, the oblique angle is defined by the panel tilt angle, and the attitude angle was determined by the roll angle of the projectile. Controlling the test setup with these two variables provided all of the desired face, edge, and corner impact conditions.
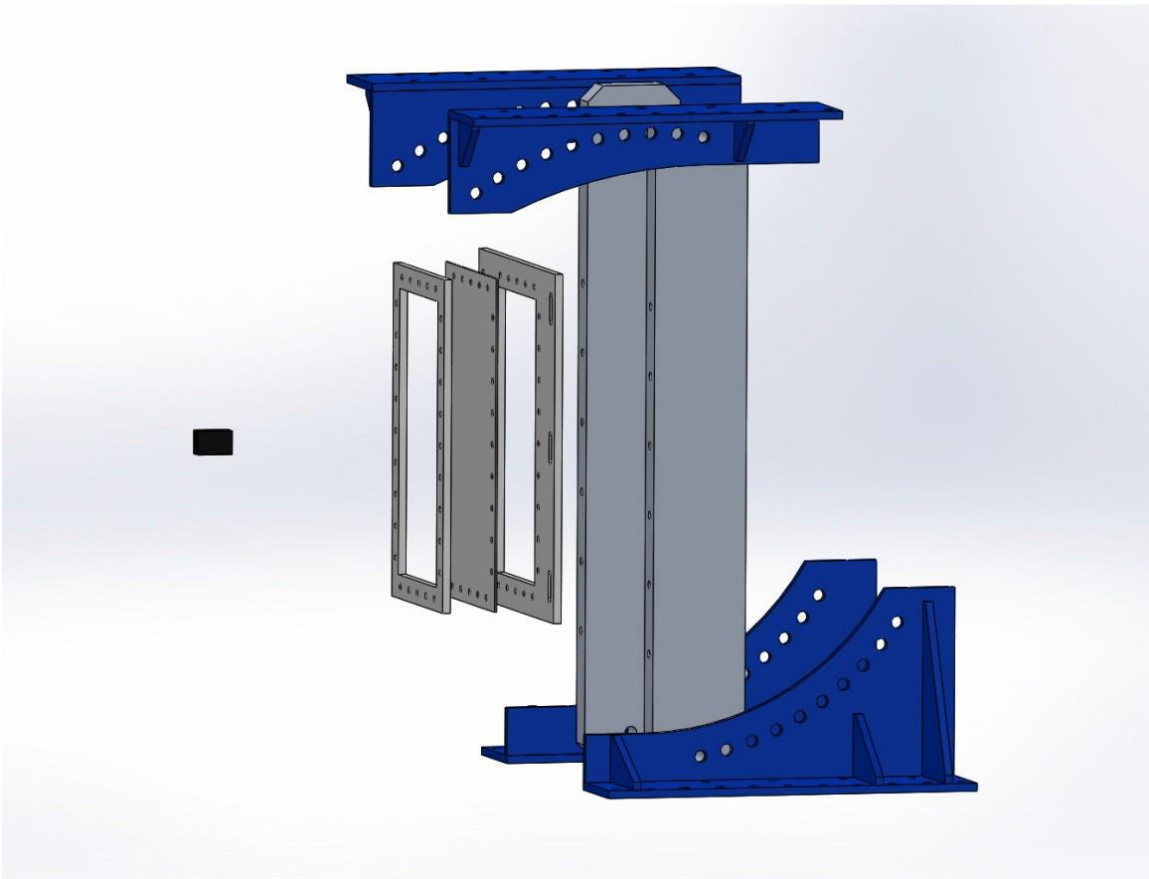
Figure 4. Exploded view of test setup [7]

Table 1. Summary of ballistic impact tests [7]

Test Setup No.	Test ID	Impact Location of Panel	Panel Tilt (Oblique) Angle (deg.)	Projectile Roll (Attitude) Angle (deg.)	Measured Impact Velocity (fps)	Measured Exit Velocity (fps)	Measured Pre-impact Projectile Roll Angle (deg.)	Measured Pre-impact Projectile Pitch Angle (deg.)	Measured Pre-impact Projectile Yaw Angle (deg.)	Comments
6.1.1	DB196		0	0	209.5		1.82	0.11	0.94	No Penetration
	DB197				211.5	-	2.89	-0.65	-0.43	No Penetration
	DB198				270.9		-0.33	2.27	-2.08	No Penetration. Crack.
	DB200				319.0		-2.90	1.70	1.05	Projectile lodged in panel
	DB199				342.0	167.0	-0.01	-1.53	-2.83	Penetration
6.2.1	DB215			0	179.2	-	-4.49	-0.58	1.62	No Penetration
	DB213				205.7		-0.03	-1.22	0.43	No Penetration. Flap.
	DB205				274.8	86.7	2.05	3.13	-1.55	Penetration
	DB214				318.7	N/A	Not Measured			Penetration
6.2.2	DB204		45	30	159.9	-	33.06	0.99	0.74	No Penetration. Corner Petal.
	DB216				172.9		24.92	0.26	3.33	No Penetration. Corner Flap
	DB203				228.0	68.9	30.26	4.21	-1.23	Penetration
	DB202				270.6	132.7	29.13	4.10	0.77	Penetration
	DB201				319.5	213.7	30.22	0.61	-1.38	Penetration
6.2.3	DB212	Off-Center		60	155.0		58.14	0.60	1.15	No Penetration
	DB211				161.7	-	60.24	3.38	-5.20	No Penetration
	DB209				200.6		64.85	-4.45	6.25	No Penetration. Hole.
	DB208				270.4	151.6	55.95	2.45	-2.79	Penetration
	DB210				317.4	216.4	60.85	-2.98	2.65	Penetration
6,2,4	DB206			90	277.0	-	90.76	-3.22	-1.28	No Penetration. Crack.
	DB207				322.5	185.0	92.11	-3.39	-2.33	Penetration
6,2,5	DB219			0	146.4	-	-4.55	-1.24	2.00	No Penetration
	DB218				203.4	2.5	-1.01	-1.13	0.65	Penetration
	DB217				269.6	169.9	1.78	1.03	3.89	Penetration
6.2.6	N/A			30	Not Tested					
6.2.7	DB222		30	60	145.9	-	61.50	-8.12	5.31	No Penetration. Perforation.
	DB221				200.3	77.9	59.49	-2.43	5.41	Penetration
	DB220				268.3	191.5	61.32	-4.27	5.26	Penetration
6.2.8	DB225			90	143.2		87.95	0.14	-1.41	No Penetration
	DB224				208.4	-	88.61	2.58	1.90	Projectile Exited Vertically
	DB223				263.8	162.5	94.79	2.79	0.23	Penetration
7.1.1	DB226	Center	0	0	262.5	-	-3.01	2.02	1.20	No Penetration
	DB227				310.2	20.0	Not Measured			Penetration. Large Flap
7.1.2	DB228			60	266.1	-	62.55	-1.07	2.59	No Penetration
	DB229				312.1	134.4	67.62	-14.36	14.02	Penetration

During the impact tests, the pre-impact velocity and projectile orientation angles, and exit velocities of the projectile were measured. Table 1 summarizes these data. In Table 1, the term "penetration" refers to the situation in which the projectile travels fully through the panel and exits the other side. The term "no penetration" refers to situations in which the projectile either ricochets away from the panel with no target plate fracture or penetration, fractures the panel but then ricochets without fully penetrating and exiting the back side, or gets lodged in the panel. Appendix B shows the photos of the plate deformation for each test.

The projectiles were accelerated to the test condition's initial velocity with a helium gas gun that was connected to a vacuum chamber containing the target plate. The projectile was carried down the gun barrel in a cylindrical polycarbonate sabot. The sabot was stopped at the end of the gun barrel by a stopper plate with a through-hole large enough to allow the projectile to pass without making any contacts with the catcher. Since there will be minor orientation variations of the projectile in the sabot, including the sabot roll angle in the gun and friction as the projectile exits the sabot, the angle at which the projectile exits the gun and first makes contact with the target cannot be perfectly controlled. This results in some test-to-test variations in obliquity and projectile attitude. The actual roll, pitch, and yaw angles of the projectile were measured during each test, as summarized in Table 1. It can be observed that the range of projectile angle deviation from test intent varies up to about 15º. The sensitivity of the projectile angle variation will be studied in Section 7.

The ballistic limit velocity is the threshold velocity required for a particular projectile to fully penetrate a particular piece of material with zero residual (exit) velocity. Figure 3.3Figure 5 shows the exit velocities of the projectile in the tests. The ballistic limit velocity ranges can be estimated from the plot. It shows how the combination of panel tilt angle and projectile roll angle affects the ballistic limit velocity of the projectile. There is a large difference in the ballistic limit velocity between the various combinations. The normal impact case has the highest ballistic limit velocity and the 30º panel tilt combinations show the lowest ballistic limit velocity, with the 45º panel tilt combinations intermediate between the two.
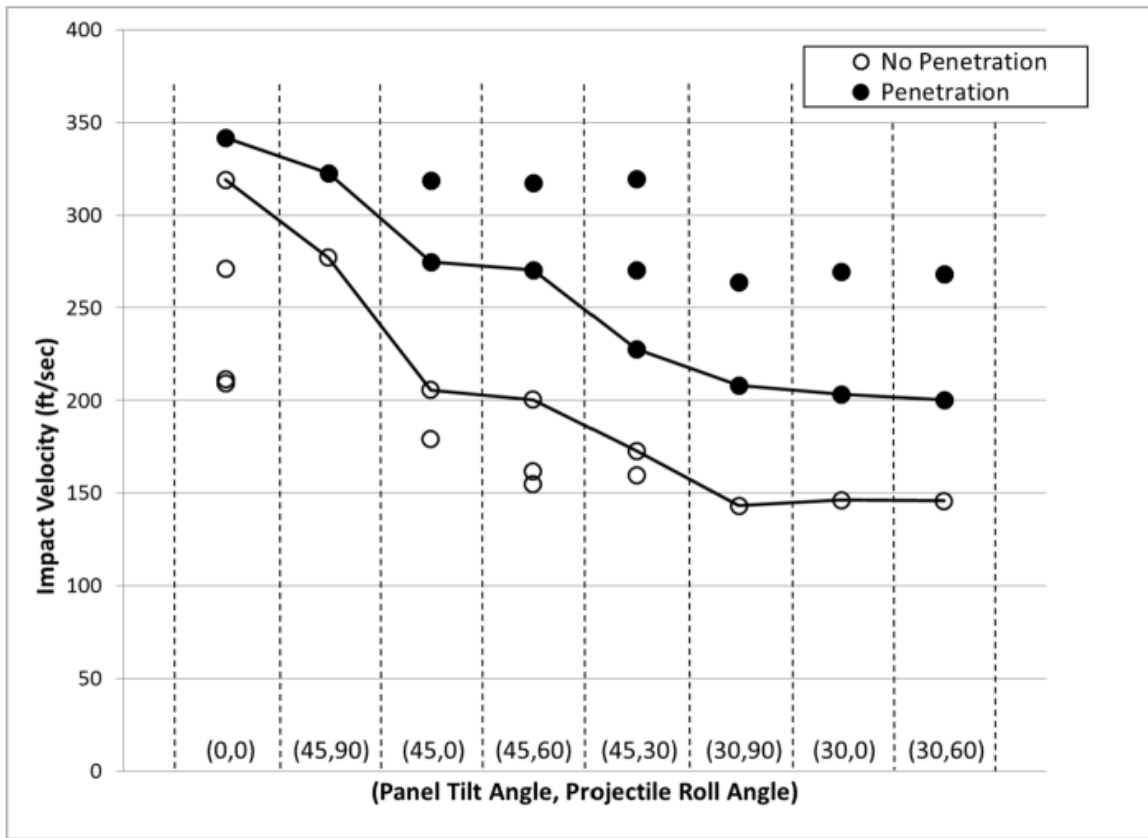
Figure 5. Range of ballistic limit velocities in tests [7]

4. *MAT_224 MODEL OF ALUMINUM 2024 ALLOY

The LS-DYNA constitutive material model *MAT_TABULATED_JOHNSON_COOK, or simply *MAT_224, was developed and subsequently updated [2, 3]. Table 2 describes the input parameters of *MAT_224. *MAT_224 is an elasto-visco-plastic material with arbitrary stress versus strain curves to define material plasticity, including arbitrary strain rate and temperature dependency. Adiabatic heating due to plastic work can cause temperatures to increase and the material to soften. Element erosion is included using plastic failure strain as a criterion, and can be defined as a function of the state of stress, strain rate, temperature, and element size. This material model resembles the original Johnson-Cook material (*MAT_015 in LS-DYNA) using similar separation of parameter dependencies, but with the possibility of general tabulated input parameters. The tabulated input parameters allow for a much closer match to mechanical property test data than the Johnson-Cook model, which is limited by curve fitting of the test data. In addition, *MAT_224 allows for parameter dependency of the Taylor-Quinney coefficient and regularization to reduce the mesh dependency of element erosion, the lack of which also limited the original Johnson-Cook model.

Table 2. Description of *MAT_224[3] and its input parameters of Aluminum 2024 alloy (units: millimeter, second, metric ton, Newton, and Kelvin)

Column	1	2	3	4	5	6	7
Card1	MID	RO	E	PR	CP	TR	BETA
Input (unit)	-	2.6E-9 (ton/mm^3)	70,000.0 (MPa)	0.3	9.0E+8 (kJoules/ ton-Kelvin)	300.0 (Kelvin)	0.4
Card2	LCK1	LCT	LCF	LCG	LCH	LCI	
Input	Table	Table	Table	Curve	Curve	Table	

MID: Material identification

RO: Mass density

E: Young's modulus

PR: Poisson's ratio

CP: Specific heat

TR: Room temperature

BETA: Fraction of plastic work converted into heat, Taylor–Quinney coefficient

LCK1: Table ID defines for each plastic strain rate value a load curve ID giving the (isothermal) effective stress versus effective plastic strain for that rate

LCT: Table ID defining for each temperature value a load curve ID giving the (quasi-static) effective stress versus effective plastic strain for that temperature

LCF: Table ID defines for each Lode parameter a load curve ID giving the plastic failure strain versus triaxiality for that Lode parameter

LCG: Load curve ID defining plastic failure strain (or scale factor) as a function of plastic strain rate. If the first abscissa value in the curve corresponds to a negative strain rate, LS-DYNA assumes that the natural logarithm of the strain rate value is used for all abscissa values

LCH: Load curve ID defining plastic failure strain (or scale factor) as a function of temperature

LCI: Table ID defines for each triaxiality a load curve ID giving the plastic failure strain versus element size for that triaxiality. If a three-dimensional table ID is referred, plastic failure strain can be a function of Lode parameter (TABLE_3D), triaxiality (TABLE), and element size (CURVE)

A general form of the hypo-elastic relation is given by

$$\boldsymbol{\sigma}^{\nabla} = \boldsymbol{f}(\boldsymbol{\sigma}, \boldsymbol{D}), \tag{4.1}$$

where $\boldsymbol{\sigma}^{\nabla}$ represents any objective rate of the Cauchy stress, $\boldsymbol{\sigma}$, and $\boldsymbol{D}$ is the rate of deformation. The stress is expressed as

$$\boldsymbol{\sigma} = \boldsymbol{s}(\boldsymbol{\varepsilon}, \dot{\boldsymbol{\varepsilon}}, T), \tag{4.2}$$

where $\boldsymbol{\varepsilon}$ is the strain, $\dot{\boldsymbol{\varepsilon}}$ is the strain rate, T is the current element temperature during the simulation. The Jaumann rate of the Cauchy stress is

$$\boldsymbol{\sigma}^{\nabla J} = \boldsymbol{C}^{\sigma J} : \boldsymbol{D}, \tag{4.3}$$

where the Jaumann rate elastic moduli $\boldsymbol{C}^{\sigma J}$ is expressed as

$$\boldsymbol{C}^{\sigma J} = \lambda \boldsymbol{I} \otimes \boldsymbol{I} + 2\mu \boldsymbol{I}, \tag{4.4}$$

where λ and μ are the Lamé constants, and $\boldsymbol{I}$ is the unit tensor. The Young's modulus, E, and the Poisson's ratio, ν, are converted by

$$E = \frac{\mu(3\lambda + 2\mu)}{\lambda + \mu}, \text{ and } \nu = \frac{\lambda}{2(\lambda + \mu)}. \tag{4.5}$$

The flow stress, σ_y, in the plastic region is expressed as

$$\sigma_y = k_1(\varepsilon_p, \dot{\varepsilon}_p) \frac{k_t(\varepsilon_p, T)}{k_t(\varepsilon_p, T_R)}, \tag{4.6}$$

where $k_1(\varepsilon_p, \dot{\varepsilon}_p)$ is the rate dependent hardening curves (defined as LCK1 in *MAT_224), $k_t(\varepsilon_p, T)$ is the temperature dependent hardening curves (defined as LCKT in *MAT_224), ε_p is the plastic strain, $\dot{\varepsilon}_p$ is the plastic strain rate, T is the temperature, and T_R is the room temperature.

The plastic failure strain is defined as

$$\varepsilon_p^f = f(\sigma^*, L) \, g(\dot{\varepsilon}_p) \, h(T) \, i(l_c, \sigma^*, L), \tag{4.7}$$

where $f(\sigma^*, L)$ is the plastic failure function (defined as LCF in *MAT_224) in the triaxiality (σ^*) and Lode parameter (L), $g(\dot{\varepsilon}_p)$ is the rate-dependent scale curve (defined as LCG in *MAT_224), $h(T)$ is the temperature-dependent scale curve (defined as LCH in *MAT_224), and $i(l_c, \sigma^*, L)$ is the element size-dependent scale function (defined as LCI in *MAT_224) in the triaxiality (σ^*) and Lode parameter (L) where l_c is the initial element size, so called characteristic length of an element. The triaxiality (σ^*) is defined as

$$\sigma^* = \sigma_m/\sigma_{VM}, \tag{4.8}$$

where σ_m is the hydrostatic stress and σ_{VM} is the Von Mises stress. The Lode parameter (*L*) is defined as

$$L = 27J_3/2\sigma_{VM}^3, \tag{4.9}$$

where J_3 is the third invariant of deviatoric stress.

Temperature increase as a result of plastic work is calculated by

$$T = T_R + \frac{\beta}{C_p\rho}\int \sigma_y\,\dot{\varepsilon}_p dt, \tag{4.10}$$

where β is the percentage of plastic work converted into heat energy (the Taylor-Quinney coefficient), C_p is the specific heat, and ρ is the density.

The previously developed Aluminum 2024 alloy *MAT_224 input parameters (Version 1.3) did not produce simulations that accurately matched the initial set of ballistic impact tests. This material model was based on data from extensive tests performed by OSU [2, 4]. However, continuing research in the development of material models for Titanium 6Al-4V and Inconel 718 alloys revealed deficiencies in the original Aluminum mechanical test data. New test methods were developed that provide additional model calibration points on the failure surface. Improved measurement techniques in material tests also were later developed. In order to correct the original model, and to include the improvements and new findings from the OSU testing, GMU re-developed the Aluminum 2024-T351 *MAT_224 material model.

OSU conducted a large number of material tests to develop the Aluminum 2024-T351 alloy material dataset required for the *MAT_224 material model. In this work, material tests were conducted with various strain rates, temperatures, specimen geometries, and loading conditions. The test series include temperature test series (tension only), rate test series (tension and compression), and failure test series (multiple stress states). The failure test series identify failure strains at different states of stress, which are achieved using different specimen geometries. The failure test program include plane stress series, axisymmetric series, plane strain series, combined loading series, and punch test series. The details of all the material tests are described in references [4, 6, 8].

Table 2 shows the *MAT_224 input parameters (Version 2.0) for the Aluminum 2024 alloy. The coefficients are presented in SI units, which are millimeter, second, metric ton, Newton, and Kelvin. The primary input parameters, such as Beta, and the LCK1, LCT, LCF, LCG, LCH, and LCI tables, which control the material model's behavior, were developed using data from tests conducted at OSU. The curves for the LCK1, LCT, LCF, LCG, LCH, and LCI are shown in Figure 6 through Figure 11, and were significantly revised from the previous version [2]. The *MAT_224 of the Aluminum 2024 alloy was validated by ballistic impact simulations of spherical and cylindrical projectiles impacting perpendicular to plates of various thicknesses, at various projectile velocities.

The validation exercise found good agreement between tests and simulations across the range of conditions tested. Demonstration of the validation agreement and details for the material model development are described in reference [6].
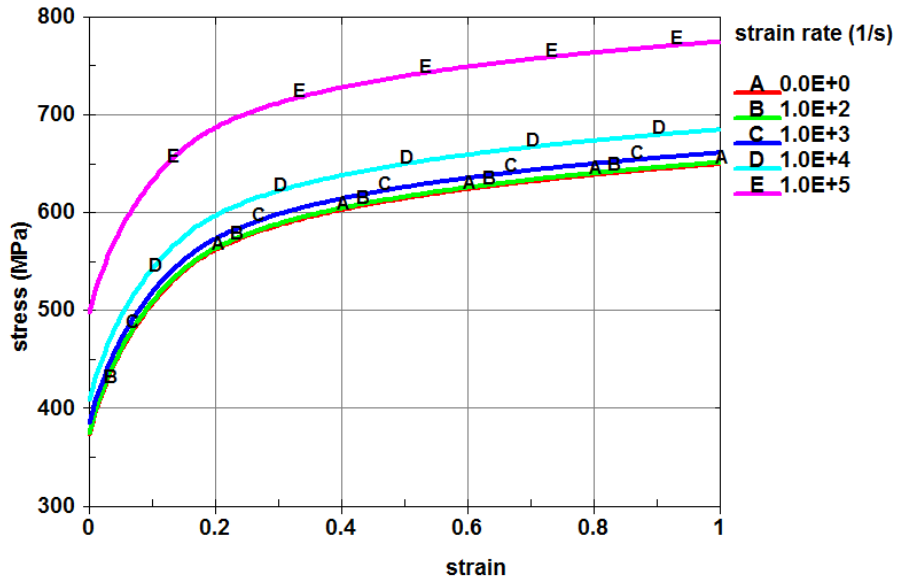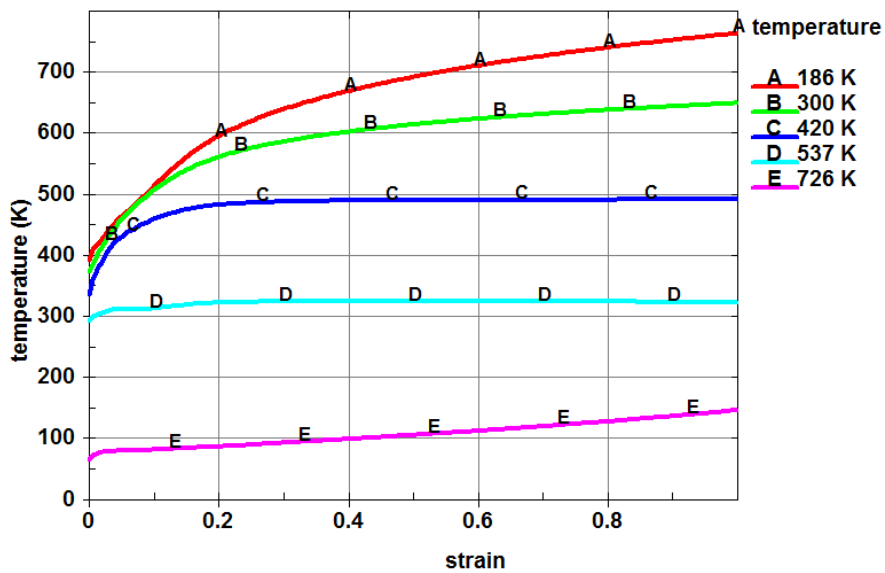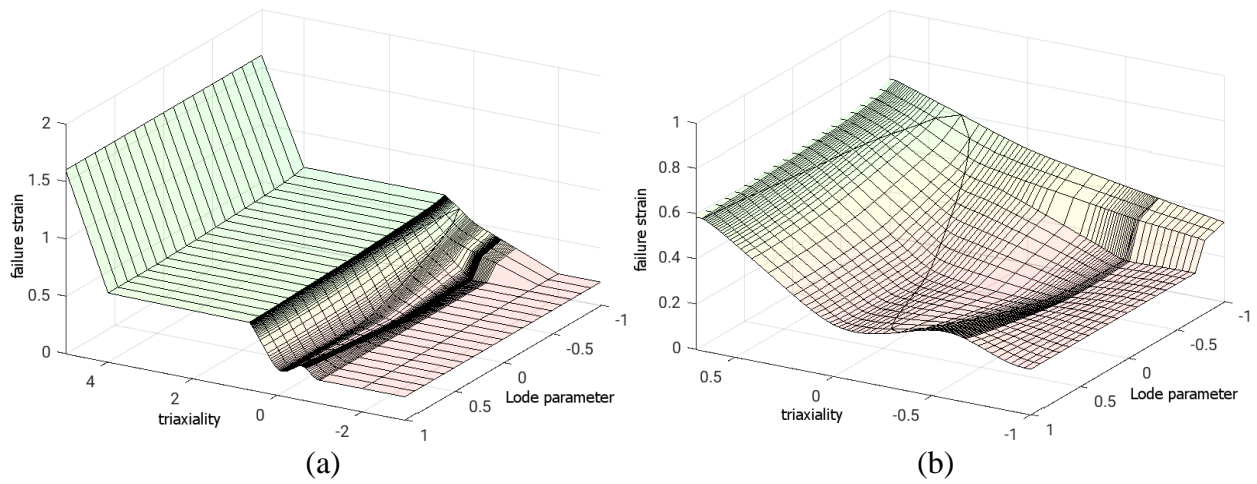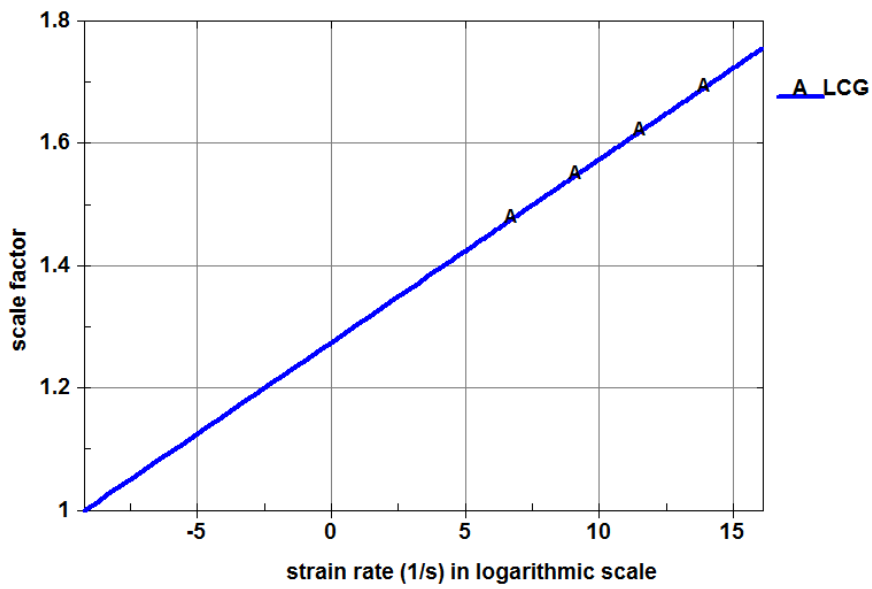

Figure 6. LCK1 of *MAT_224

Figure 7. LCT of *MAT_224

Figure 8. LCF of *MAT_224: (a) full range of Triaxiality and (b) magnifying the range of $-1.0 \leq \text{Triaxiality} \leq 0.7$
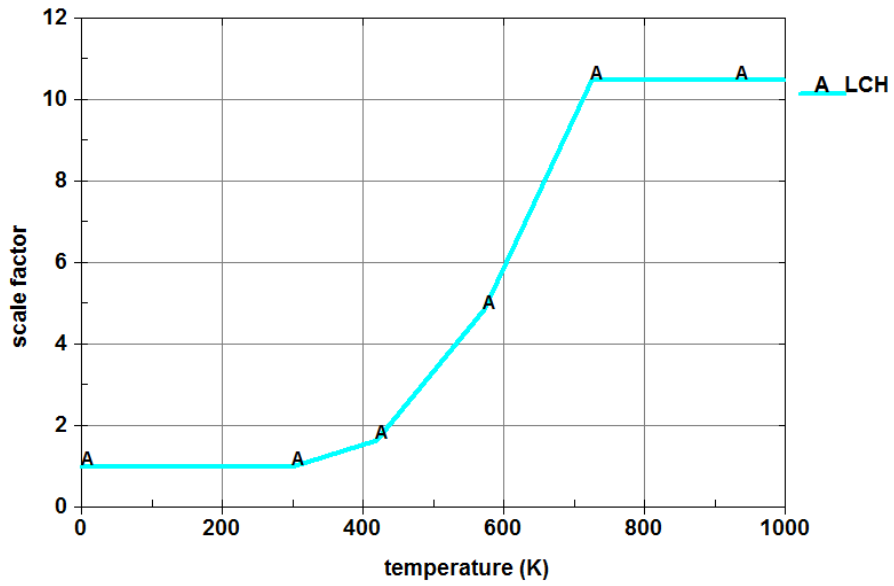

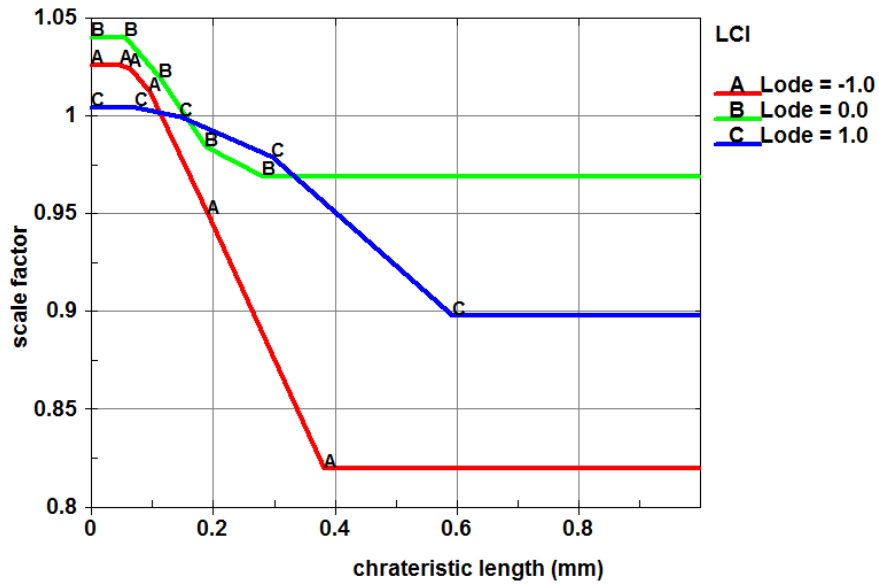**Figure 9. LCG of *MAT_224**

Figure 10. LCH of *MAT_224

Figure 11. LCI of *MAT_224

18

5. BALLISTIC IMPACT FINITE ELEMENT MODEL

Figure 12 shows the Finite Element (FE) models of the Inconel projectile and the Aluminum plate developed in LS-DYNA. These models were created using all solid elements. The fixture supporting the target plate was not modeled because the size of the projectile is much smaller than the impact surface of the plate, and the impact location on the plate is far enough away from the plate boundary to make fixture boundary effects inconsequential relative to the ballistic impact simulations. In addition, not modeling the fixture hardware helps reduce the number of elements in the overall system model. For all simulations, the plate edge boundaries were all fixed. The two target cross-points shown in Figure 12(b) indicate the two different projectile impact points (center and off-center) used during testing.

(a)

(b)
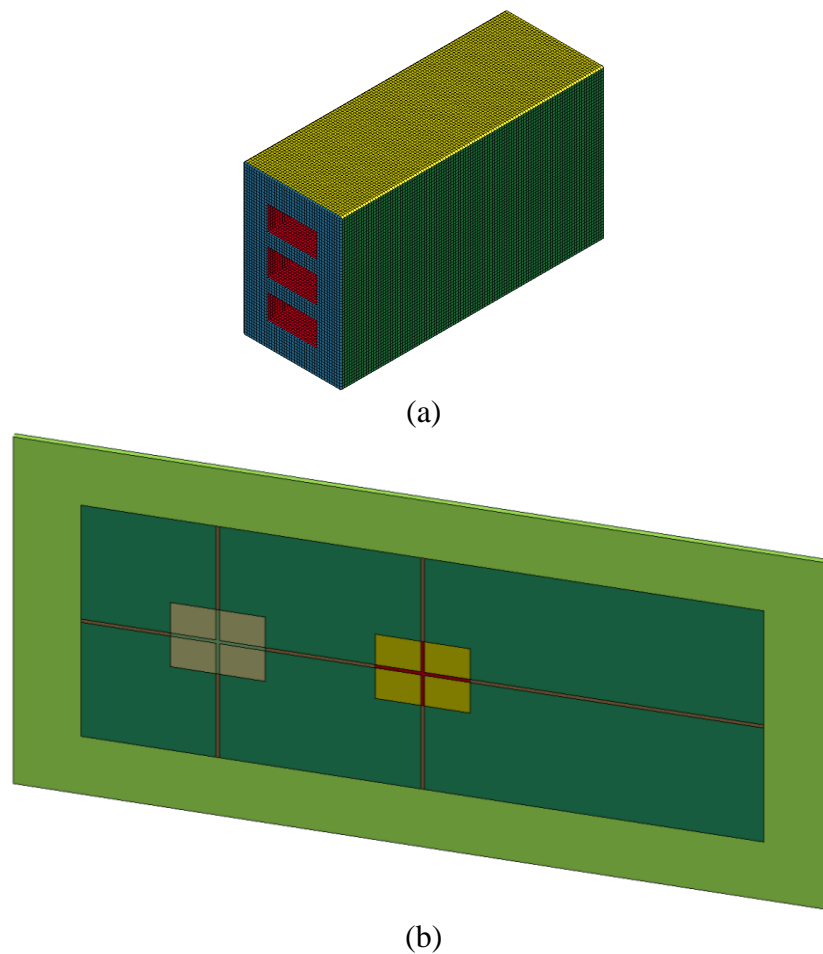
Figure 12. FE models: (a) projectile and (b) plate

The *MAT_224 material model (Version 2.0) for Aluminum 2024 described in Section 4 was used to model plastic material failure behavior for the target plates. The *MAT_224 material model [9] for Inconel 718, which has a complete plasticity definition and failure model undefined, was used for the projectile. Ignoring failure in the Inconel projectile is acceptable because it was shown

during test and initial model development that the deformation of the projectile was negligible in the ballistic impact tests, and there was no projectile erosion.

Before conducting test simulations, sensitivity studies for the target plate model were conducted in order to select the appropriate modeling detail baseline for the plate model. First, the mesh sensitivity was studied. Four different element sizes, based on the number of elements through the plate thickness, were selected. The four different element sizes were: (1) 3 elements through the plate thickness (1.04 mm); (2) 6 elements (0.52 mm); (3) 12 elements (0.26 mm); and (4) 24 elements (0.13 mm). Figure 11 shows that the *MAT_224 dataset for the Aluminum 2024 has the mesh regularization curves (LCI). This LCI table was developed using various element sizes within the range of 0.03 mm to 0.4 mm. It can be noted that the element sizes of 3-element and 6-element models are out of the regularization range. Those of 12-element and 24-element models are within the regularization range.

The numerical sensitivity studies were performed using simulations of test setup #7.1.1, shown in Table 1, to guide modeling practices. In #7.1.1, the projectile impacts the center of the plate with 0º panel tilt angle and 0º projectile roll angle. This allows for the use of a quarter symmetry model that reduced computer runtime significantly. Figure 13 shows the quarter symmetry model. The total numbers of solid elements used in the simulation models for the four different element sizes are about 0.08 million (3 elements through the plate thickness), 0.65 million (6 elements), 5.2 million (12 elements), and 41.6 million (24 elements). The initial impact velocity of the projectile was set to 400 fps for all simulations.
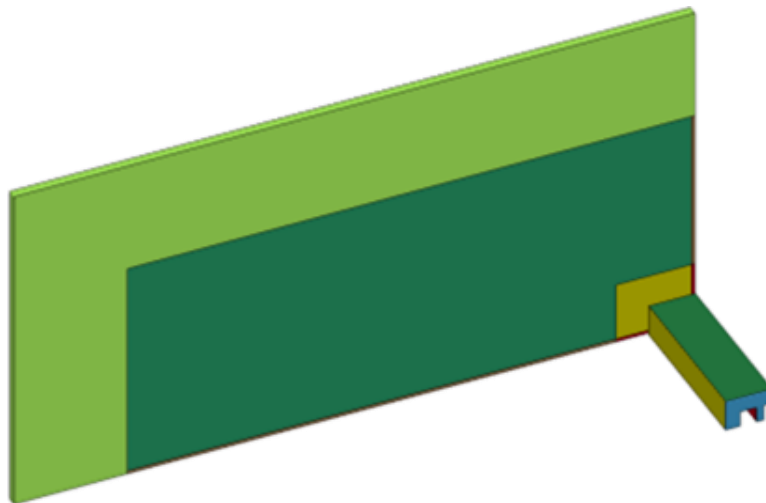
Figure 13. Quarter symmetry model of test setup #7.1.1

Two different integration schemes—full integration and reduced integration—were selected for the solid elements. The *MAT_224 dataset for Aluminum 2024 was developed using full integration. However, since the ballistic impact simulations required a very large number of solid elements, excessive computation time resulted. To improve performance, the reduced integration scheme was tested to see if it could provide reduced runtime and results with comparable accuracy. In addition, the sensitivity of the LS-DYNA MPP solver, implemented on a High Performance

20

Computing (HPC) platform, was studied by performing the same simulation on two different HPC clusters, using different numbers of cluster nodes in the clusters. Not all possible parameter combinations were conducted in the sensitivity studies. Table 3 summarizes the 12 selected combinations performed.

Table 3 details the projectile exit velocities for the element-size sensitivity study. First, the effect of mesh size can be seen as the projectile exit velocity increases with decreasing element size. The exit velocity converges in the range of 309 fps to 314 fps when the element size is 0.26 mm (12 elements through plate thickness) and 0.13 mm (24 elements), both of which are within the regularization range of the *MAT_224 Aluminum material model. The models with the larger element sizes, which are outside of the regularization range, do not produce accurate ballistic impact simulation results. An additional contribution to the inaccuracy of the larger element sizes is that the stress predictions may not have reached convergence.

Second, ballistic simulations for 12 elements through the thickness, performed using two different clusters (GMU/CCSA cluster and FAA cluster) and different numbers of nodes (1, 2, and 4 nodes) show very close exit velocity correlation. This demonstrates that the ballistic impact simulation is not sensitive to HPC machine types.

Finally, Table 3 shows that the selection of full vs. reduced integration does have an effect on exit velocity predictions. In the simulations with 12 elements through the target thickness, the exit velocity with reduced integration is about 7% less than that with full integration. However, when assessed against runtime, the 7% error for reduced integration was found to be an acceptable and necessary trade, since it reduces runtime three- to four-fold.

Based on these results, it was decided that all ballistic impact simulation models for the general obliquity study would be conducted with the 0.26 mm element size (12 elements through the plate thickness) and reduced element integration scheme.

Table 3. Summary of exit velocities of the projectile in simulation model sensitivity studies

GMU/CCSA cluster (16 CPUs/node)			
Number of elements through plate thickness (element size)	nodes	Exit velocity of the projectile	
		Full integration	Reduced integration
3 elements (1.04 mm)	1 node	241.7 fps	No penetration
6 elements (0.52 mm)	1 node	289.2 fps	261.7 fps
12 elements (0.26 mm)	1 node	314.2 fps	291.7 fps
FAA cluster (28 CPUs/node)			
Number of elements through plate thickness (element size)	nodes	Exit velocity of the projectile	
		Full integration	Reduced integration
12 elements (0.26 mm)	1 node	313.3 fps	N/A
	2 nodes	313.3 fps	290.8 fps
	4 nodes	313.3 fps	N/A
24 elements (0.13 mm)	3 nodes	N/A	295.8 fps
	4 nodes	309.2 fps	N/A

6. BALLISTIC IMPACT SIMULATION

The ballistic impact simulations for the 11 different test setups shown in Table 1 were conducted with a range of impact velocities to identify the ballistic limit and residual velocities of the projectile in those test conditions. The ballistic limit velocity is the velocity at which the projectile will fully penetrate the target panel with zero residual velocity. To find the ballistic limit for a given test setup, the initial impact velocity of the projectile was varied from 150 fps to 400 fps in 50 fps intervals. As in the sensitivity study, in order to reduce simulation runtime, an appropriate symmetry model was used, if the symmetry assumption was applicable. The quarter symmetry model was used for test setup #7.1.1. The half symmetry model was used for #6.1.1, #6.2.1, #6.2.4, #6.2.5, and #6.2.8, and the full model had to be used for #6.2.2, #6.2.3, #6.2.6, #6.2.7, and #7.1.2. The quarter symmetry, half symmetry, and full models contain approximately 5 million, 10 million, and 20 million solid elements, respectively. Table A-1 in Appendix A summarizes all the simulations.

Appendix B shows the initial test setups, plots with exit velocities of the projectile, plate deformations in tests, and plate deformations in simulations of all 11 test conditions. The initial setups in Figure B-1(a) ~ Figure B-11(a) show the impact location of the projectile on the plate and the impact flight configurations of the projectile for the assigned panel tilt angle and projectile roll angle. In all cases, the impact direction of the projectile to the plate is parallel to the long edge of the rectangular projectile.

The plots in Figure B-1(b) ~ Figure B-11(b) show the exit velocities as a function of initial velocity for the range of initial impact velocities in the tests (blue squares) and simulations (red triangles). The reference line (red dotted line) bounds the results with a no-velocity-change ceiling. The fitting lines through the data points of exit velocities in simulations were determined based on a

generalization of an analytical model originally proposed by Recht and Ipson [10]. The equation of residual velocities is expressed as

$$v_r = a(v_i{}^p - v_{bl}{}^p)^{1/p},$$

(6.1)

where v_r is the residual (or exit) velocity, v_i is the initial velocity, v_{bl} is the ballistic limit velocity, and a and p are empirical constants derived from curve fitting of impact data [11]. The fit curve (green line) over the projectile exit velocities in simulations was approximated by finding the combination of parameters (ballistic limit velocity and empirical constants) in Equation (6.1) that minimize the Root Mean Square (RMS) error. The curve fitting parameters are summarized in Table A-1.

Figure B-1(c) ~ Figure B-11(c) show the plate deformations in tests, as referenced in the NASA report [7]. The upper photos of the front and back sides of the plate are from no-penetration tests and the lower photos are from penetration tests. The Test ID number, with the initial impact velocity of the projectile in parentheses, is shown under the photos. Figure B-1(d) ~ Figure B-11(d) show the comparable images of the plate deformation in the simulations. The initial impact velocity of the projectile is shown in that image.

The impact configurations of the 11 test setups can be classified as face, edge and, corner impact cases, based on the initial contact geometry of the projectile as it contacts the plate. Basically, ballistic tests with the same impact configuration show similar penetration processes and failure modes.

6.1 Face impact cases

The face impact cases include test setups #6.1.1, #7.1.1, and #7.1.2 in Table 1. In the face impact cases, the front face of the rectangular projectile initially contacts the surface of the plate.

Test setup #6.1.1 is the face impact test with 0º oblique angle and 0º projectile roll angle. The projectile impacts the off-center position of the plate, as shown in Figure B-1(a). The projectile exit velocities, with respect to the initial impact velocities in the simulations, are very closely matched with the test points, as shown in Figure B-1(b). In the tests, the projectile penetrated the plate by shearing (cutting) with a part of the contact edges of the front face of the projectile and by petaling the plate with another part of the contact edges, as shown in Figure B-1(c). In the simulations, the projectile penetrates the plate by shearing with the contact edges of the front face of the projectile, but mostly without producing any petals, as shown in Figure B-1(d), which is different from the tests. Figure B-1(d) illustrates a crooked cut in the cut edges of the plate, which indicates that the failure propagation deviated from the cutting edge of the projectile at that point, but returns to follow the cutting edge soon after.

The petaling in the tests is produced by crack propagation. Stress concentrations at a propagating crack front are extremely high. As a result, accurate crack propagation simulation, when not caused by immediate contact with the projectile, often requires an extremely fine mesh. Elements an order of magnitude, or more, smaller than studied in the sensitivity analysis may be required. In addition,

petaling patterns in tests, away from a projectile edge, may be somewhat random. They depend on small variations in initial conditions and material properties, especially in the face impact cases. As post-rupture petaling has a lesser effect on the ballistic limit and exit velocities, no attempt to improve the match to the test petaling patterns in the face impact cases was made. A future study could be performed to improve understanding of mesh sensitivity.

Test setup #7.1.1 is the face impact test with 0º oblique angle and 0º projectile roll angle. The projectile impacts the center of the plate as shown in Figure B-10(a). The projectile exit velocities, with respect to the initial impact velocities in the simulations, are very closely matched with the test points, as shown in Figure B-10(b). In the tests, the projectile penetrated the plate by shearing with a part of the contact edges of the front face of the projectile and producing petals, as shown in Figure B-10(c). In the simulations, the projectile penetrates the plate by cutting with the contact edges of the front face of the projectile without producing any petals, as shown in Figure B-10(d), which is different from the tests. The difference between test setups #6.1.1 and #7.1.1 is the impact point of the projectile on the plate; #6.1.1 is off-center and #7.1.1 is in the center of the plate. The results in both tests and simulations are very similar.

Test setup #7.1.2 is the face impact test with 0º oblique angle and 60º projectile roll angle. The projectile impacts the center of the plate as shown in Figure B-11(a). The projectile exit velocities, with respect to the initial impact velocities in the simulations, are lower than the test points, as shown in Figure B-11(b). In Table 1, the measured roll, pitch, and yaw angles of the projectile in DB229 range from 7.6º to 14.4º. This large angle deviation in the test could have caused the discrepancy in the projectile exit velocity between tests and simulations. Another cause might be the mismatch of the mesh patterns between the contact surfaces of the projectile and the plate, as shown in Figure 14, which requires a further study. In the tests, the projectile penetrated the plate by cutting with most of the contact edges of the projectile front face and producing slight petals, as shown in Figure B-11(c). In the simulations, the projectile penetrates the plate by shearing with the contact edges of the front face of the projectile without producing any petals, as shown in Figure B-11(d), which shows a minimal similarity with the tests. The difference between test setups #7.1.1 and #7.1.2 is the projectile roll angle; #7.1.1 has 0º projectile roll angle, and #7.1.2 has a 60º roll angle. The results in the simulations are similar to each other.
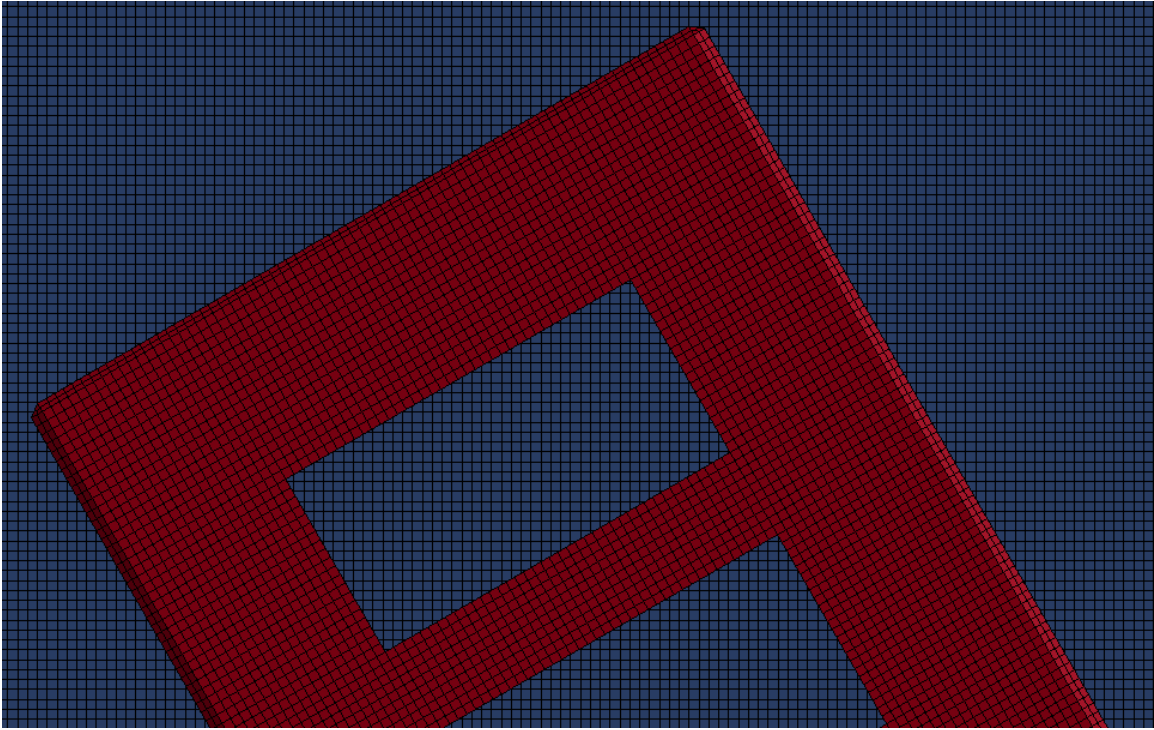
Figure 14. Mesh patterns in #7.1.2

The most noticeable difference between tests and simulations in the face impact cases is the penetration shape of the plate. Table 1 shows that there is always 2º to 3º attitude angle deviation in the face impact tests. In the face impact cases, both the projectile exit velocity and the penetration shape of the plate are very sensitive to the attitude angle deviation, which will be described more in Section 7.

6.2 Edge impact cases

The edge impact cases include test setups #6.2.1, #6.2.4, #6.2.5, and #6.2.8. In the edge impact cases, either the short or mid edge of the rectangular projectile initially contacts the surface of the plate.

Test setup #6.2.1 is the edge impact test with a 45º oblique angle and 0º projectile roll angle. The short edge of the rectangular projectile impacts the off-center location of the plate, as shown in Figure B-2(a). The projectile exit velocities, with respect to the initial impact velocities in the simulations, are very closely matched with the test points, as shown in Figure B-2(b). In the tests, the projectile penetrated the plate by cutting with the contact edge of the projectile front face, and by producing a petal at the end, as shown in Figure B-2(c). The simulations show very similar behavior and final penetration shape relative to the tests, as shown in Figure B-2(d).

Test setup #6.2.4 is the edge impact test with a 45º oblique angle and a 90º projectile roll angle. The mid-edge of the rectangular projectile impacts the off-center location of the plate, as shown in Figure B-5(a). The projectile exit velocities, with respect to the initial impact velocities in the

simulations, are very closely matched with the test points, as shown in Figure B-5(b). In the tests, the projectile penetrated the plate by shearing with the contact edge of the front face of the projectile and producing a petal, which was then torn making a V-shape, as shown in Figure B-5(c). The simulations show very similar behavior and final penetration shape of the plate relative to the tests, except for the V-shape, as shown in Figure B-5(d).

Test setup #6.2.5 is the edge impact test with a 30° oblique angle and 0° projectile roll angle. The short edge of the rectangular projectile impacts the off-center location of the plate, as shown in Figure B-6(a). The projectile exit velocities, with respect to the initial impact velocities in the simulations, match closely with the test points, as shown in Figure B-6(b). In the tests, the projectile penetrated the plate by shearing with the contact edge of the front face of the projectile and by producing a petal at the end, as shown in Figure B-6(c). The simulations show very similar behavior and final penetration shape of the target plate with respect to the tests, as shown in Figure B-6(d).

Test setup #6.2.8 is the edge impact test with a 30° oblique angle and a 90° projectile roll angle. The mid-edge of the rectangular projectile impacts the off-center location of the plate, as shown in Figure B-9(a). The projectile exit velocities, with respect to the initial impact velocities in the simulations, are very closely matched with the test points, as shown in Figure B-9(b). In the tests, the projectile penetrated the plate by shearing with the contact edge of the front face of the projectile and producing a petal, which split making a dull V-shape, as shown in Figure B-9(c). The simulations show very similar behavior and final penetration shape of the plate relative to the tests, with the exception of the attached petal, as shown in Figure B-9(d).

In the edge impact cases, the results between the tests and simulations are quite similar. The difference between the tests and simulations in these cases is the behavior of the plate petal during the final phase of the penetration process. However, the behavior of the petal was not found to be critical with respect to predicting the ballistic limit velocity of the projectile. In future research, examination of crack propagation could improve prediction of petaling and other extremely local effects.

6.3 Corner impact cases

The corner impact cases include test setups #6.2.2, #6.2.3, #6.2.6, and #6.2.7. In these cases, one of the corners of the front face of the rectangular projectile initially contacts the surface of the plate.

Test setup #6.2.2 is the corner impact test with a 45° oblique angle and a 30° projectile roll angle. The corner of the rectangular projectile impacts the off-center location of the plate, as shown in Figure B-3(a). The projectile exit velocities, with respect to the initial impact velocities in the simulations, are very closely matched with the test points, as shown in Figure B-3(b). In the tests, the projectile penetrated the plate by cutting with the contact edge of the front face of the projectile without creating any petals, as shown in Figure B-3(c). The simulations show very similar behavior and final penetration shape of the plate with the tests, as shown in Figure B-3(d).

26

Test setup #6.2.3 is the corner impact test with a 45º oblique angle and a 60º projectile roll angle. The corner of the rectangular projectile impacts the off-center location of the plate, as shown in Figure B-4(a). The projectile exit velocities, with respect to the initial impact velocity in the simulations, are a little lower than the test points, as shown in Figure B-4(b). In the tests, the projectile penetrated the plate by shearing with the contact edge of the front face of the projectile and by producing a petal, which failed when being bent into a U-shape, as shown in Figure B-4(c). The simulations show very similar behavior and final penetration shape of the plate with the tests, with the exception of the U-shape, as shown in Figure B-4(d).

Test setup #6.2.6 is the corner impact test with a 30º oblique angle and a 30º projectile roll angle. The corner of the rectangular projectile impacts the off-center location of the plate, as shown in Figure B-7(a). There is no comparable test result available for this setup. The projectile exit velocities, with respect to the initial impact velocities in the simulations, are shown in Figure B-7(b). In the simulations, the projectile penetrated the plate by shearing with the contact edge of the front face of the projectile without producing any petals, as shown in Figure B-7(d).

Test setup #6.2.7 is the corner impact test with a 30º oblique angle and a 60º projectile roll angle. The corner of the rectangular projectile impacts the off-center location of the plate, as shown in Figure B-8(a). The projectile exit velocities, with respect to the initial impact velocities in the simulations, are a little lower than the test points, as shown in Figure B-8(b). In the tests, the projectile penetrated the plate by shearing with the contact edge of the front face of the projectile and by producing a petal, which failed in bending as the projectile exited the plate, as shown in Figure B-8(c). The simulations show very similar behavior and final penetration shape of the plate with respect to the tests, except that in testing, the petal was still hanging onto the plate, as shown in Figure B-8(d). As noted in Section 6.2, future research and development could improve prediction of petaling and other extremely local effects.

In the corner impact cases, the results between the tests and simulations are quite similar. The difference between tests and simulations in these cases is that the data points for the projectile exit velocity in simulations, especially the cases with a 60º projectile roll angle, are lower than the test data points. This might be caused by the misalignment of the mesh pattern of the plate to the failure lines cut by the projectile, which is the same cause in test setup #7.1.2.

6.4 Effect of oblique and attitude angles

Figure 15 shows the estimated exit velocity curves for the projectile in all 11 test setups. Considering cases with an initial impact velocity of 400 fps, the exit velocities of the projectile are sensitive to the oblique angle, as shown in Figure 15(a). The cases with 0º oblique angle show the lowest exit velocity (282 fps – 291 fps). The cases with a 30º oblique angle show the highest exit velocity (328 fps – 333 fps). The cases with a 45º oblique angle show a mid-range of the exit velocity (291 fps – 303 fps) between the two.
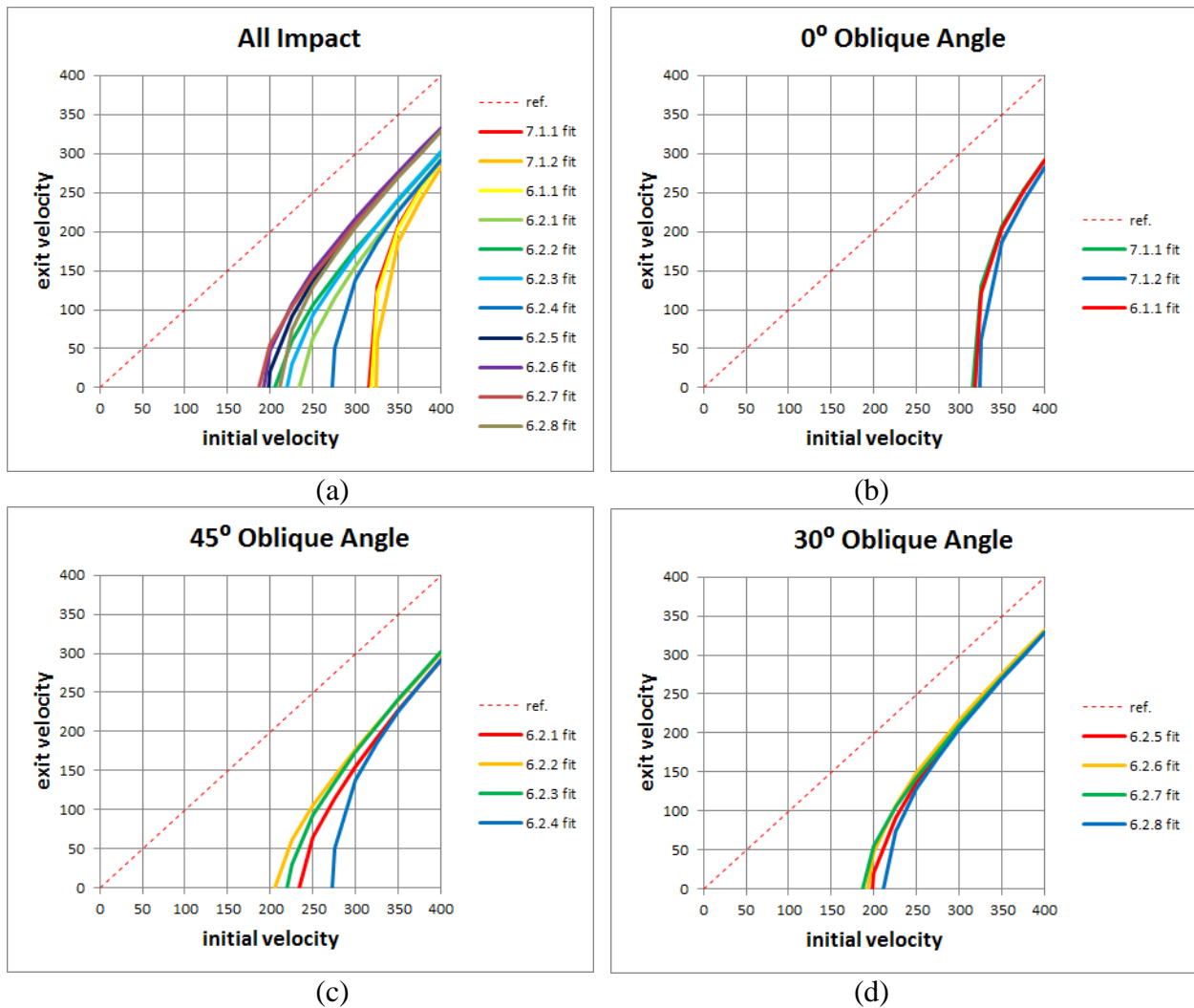
Figure 15. Estimated exit velocity curves of the projectile (unit: fps): (a) all impact cases; (b) 0º oblique angle cases; (c) 45º oblique angle cases; and (d) 30º oblique angle cases

Ballistic limit velocities are also sensitive to the projectile roll angle and impact configurations. The cases with 0º oblique angle in Figure 15(b) are the face impact cases, where the ballistic limit velocities are similar regardless of the projectile roll angles. In the cases with a 45º oblique angle in Figure 15(c), the projectile roll angle changes from 0º to 90º at 30º intervals. The corner impact cases with 30º and 60º projectile roll angles show lower ballistic limit velocities, whereas the edge impact cases with 0º and 90º projectile roll angles show the higher ballistic velocities. The cases with 30º oblique angles in Figure 15(d) are similar to the cases with 45º oblique angles. However, the cases with a 45º oblique angle show larger variation of the ballistic limit velocities than the cases with a 30º oblique angle.

Figure 16 shows the estimated ballistic limit velocities of the projectile in the simulations when inserted into Figure 5. The estimated ballistic limit velocities (green diamonds) are within the test range (between black and red triangles). The estimated ballistic limit velocity curve (green line)

28

shows how the ballistic limit velocities change as the oblique and projectile roll (or attitude) angles change.
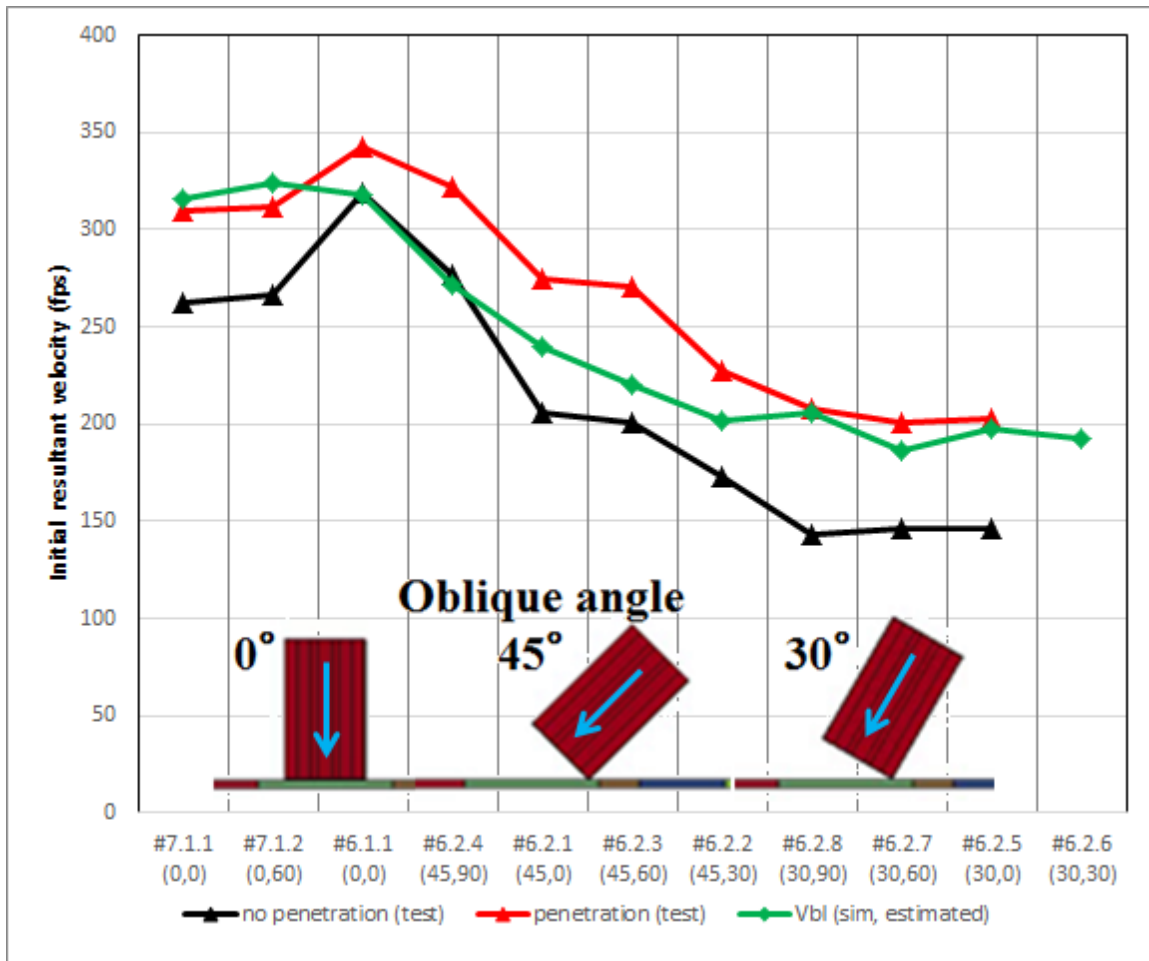
Figure 16. Ballistic limit velocities in simulations (values in the parentheses are the oblique and projectile roll angles)

7. SENSITIVITY ANALYSIS OF OBLIQUE AND ATTITUDE ANGLES IN BALLISTIC IMPACT

Since the essential accuracy of the methods and models has been established, a further trend-establishing study was undertaken, beyond the specific oblique and attitude angles that were tested. The sensitivity of exit velocities upon projectile-varying oblique and attitude angles, using the verified projectile and plate models, was studied by conducting additional simulations.

Fundamentally, there are three penetration processes in the ballistic impact that absorb impact energy and decelerate the projectile: (1) the deformation process; (2) the failure process; and (3) the frictional slide process. For a given initial velocity, the influences of these three processes vary depending on the impact configuration. In general, the deformation process absorbs a large portion of the impact energy by deforming the surrounding area at the impact location. The failure process absorbs some portion of the impact energy depending on the failure mode. The frictional slide process absorbs another portion of the impact energy depending on how the side and top faces of the projectile interact with the cut edge.

Figure 17 illustrates the penetration processes for a rectangular projectile during the ballistic impact in eight steps. The impact condition setup for this illustration has a small oblique angle to make an edge impact (Step 1). When the leading edge of the projectile contacts the target plate, the projectile deforms the contact location, causing local plastic deformation (Step 2). When the plastic deformation reaches the failure criteria, failure initiates in the plate where the short edge of the front face of the projectile contacted initially (Step 3). The failure propagates by shearing the plate with the mid-edge of the projectile front face (Steps 4 through 6). During the failure propagation process, the side face of the projectile slides past the cut edge of the plate with high frictional resistance (Steps 6 and 7). The petal is developed as the failed surface is folded back by the projectile and could detach from the plate late in the event (Step 7). Finally, the penetration process is completed as the projectile passes completely through the plate (Step 8). The velocity history of the projectile shows the deceleration of the projectile associated with the penetration process, which demonstrates the influences of the three processes.
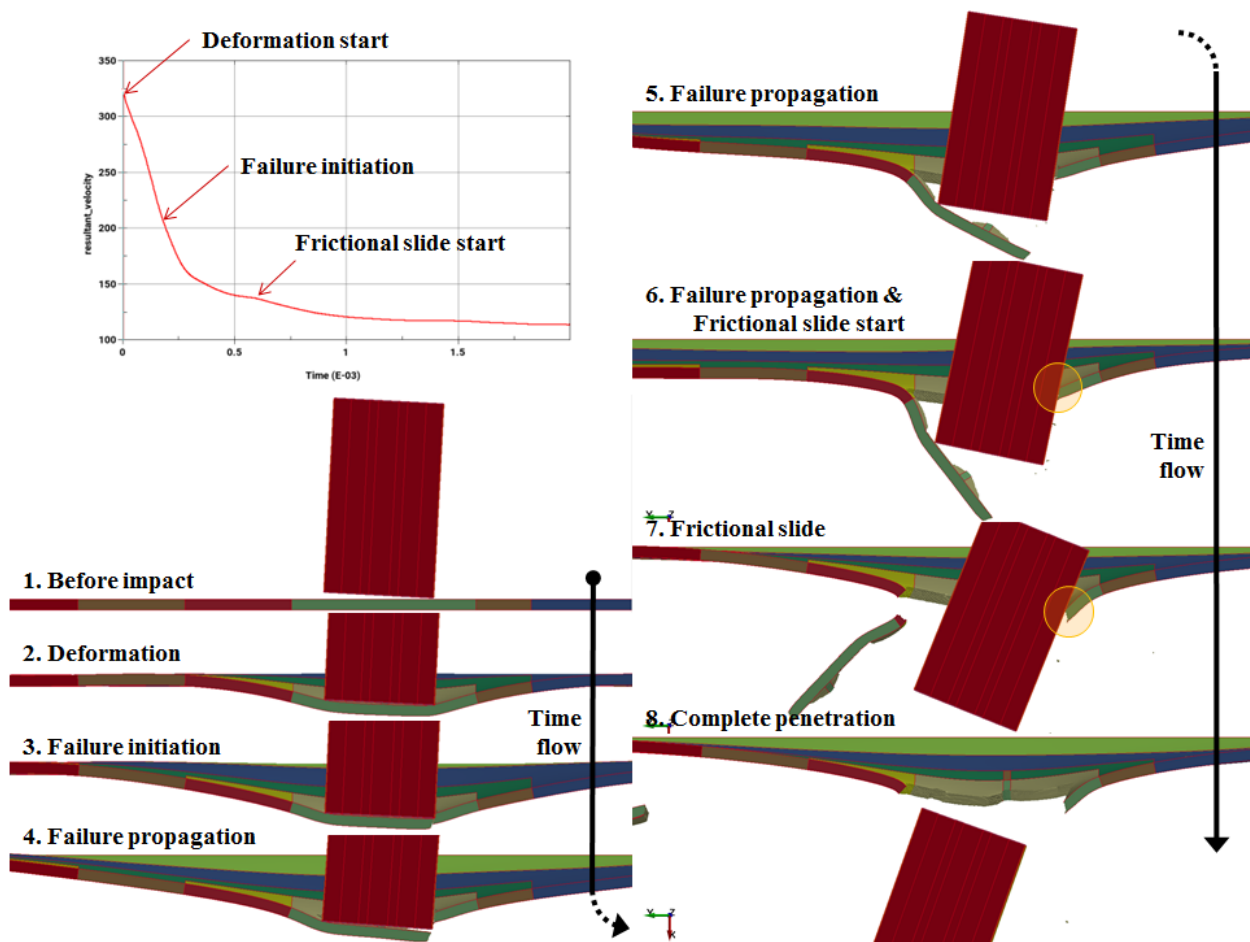
Figure 17. Penetration processes of a rectangular projectile in the ballistic impact (plot units: second vs. fps)

7.1 Oblique angle variation

In order to determine how the oblique angle affects the exit velocity of the projectile, two series of ballistic impact simulations were conducted. Starting from the baseline #6.1.1, which is the face impact, the projectile tilt angle is changed from 0º to 45º in 5º increments, resulting in a range of edge impact conditions referred to as the edge impact series. In another series, the projectile roll angle is set to 30º and then the projectile tilt angle is changed from 0º to 45º in 5º increments, referred to as the corner impact series. Figure 18 compares the initial setups of two projectiles with 0º and 30º roll angles. Figure 19 compares the initial setups of four oblique angle conditions. The initial impact velocity of the projectile in all of these simulations was set to 400 fps.
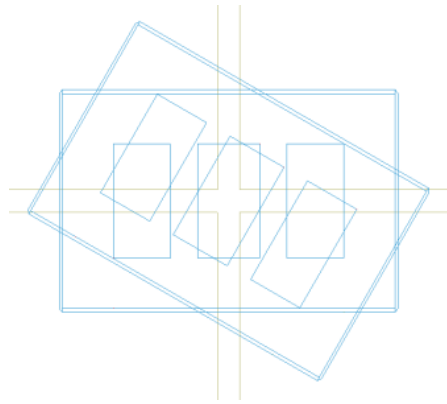
Figure 18. Overlap of the projectiles with 0º and 30º roll angles

Figure 19. Overlap of ballistic impact setups of the oblique angle variation series (blue arrows indicate the projectile flight direction)

Table 4 summarizes the exit velocities of the projectile in the two oblique angle variation series. The data points for the exit velocities are plotted in Figure 20. These results confirmed that the exit velocity of the projectile is a function of the oblique angle, and both oblique angle variation series show a very similar trend. The exit velocity of the projectile is lowest when the oblique angle is 5º, and highest when the oblique angle is 25º. The highest projectile exit velocities in the two oblique angle variation series are similar, but the lowest exit velocity in the edge impact cases is about 20 fps higher than in the corner impact cases.

Table 4. Summary of exit velocities of the projectile in two oblique angle variation series

Oblique Angle (°)	Initial Velocity (fps)	Exit Velocity (fps)			
		Edge Impact		Corner Impact	
0 (Face Impact)		290	#6.1.1	278	
5		284		265	
10		288		296	
15		308		317	
20	400	335		324	
25		340		334	
30		334	#6.2.5	332	#6.2.6
35		324		326	
40		311		317	
45		295	#6.2.1	304	#6.2.2
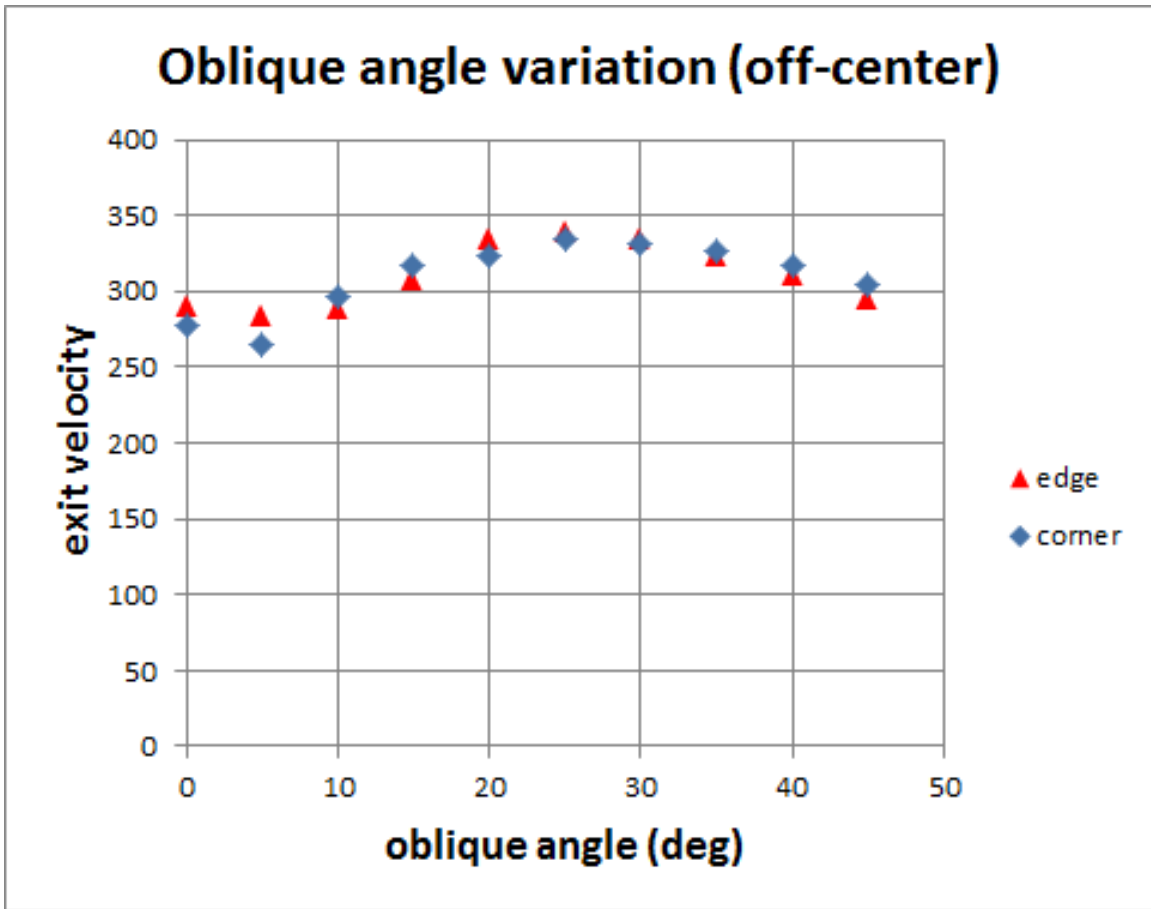
Figure 20. Plot of the exit velocities of the projectile in two oblique angle variation series

As a further description of the penetration physics with obliquity angles, two cases with different exit velocities are compared. Figure 21 compares these two cases; one with 0º roll angle, the other with a 30º roll angle. The penetration shapes of two cases are very similar, as shown in Figure 21(a) and Figure 21(b), but the projectile velocity histories of the two cases, shown in Figure 21(c), begin to differentiate after 0.1 msec. It is interesting to note that the velocity for the case with the 30º roll angle is lower than the 0º roll angle case. Figure 21(d) compares the snapshots of two cases at 0.2 msec. The snapshots were taken at the center section plane of the model. One noticeable difference between the two cases in Figure 21(d) is that the deformation of the plate by the projectile in the case with the 30º roll angle (blue) is larger than the one with 0º roll angle (red). This absorbs more impact energy and probably leads to the lower projectile exit velocity than the case with the 30º roll angle.
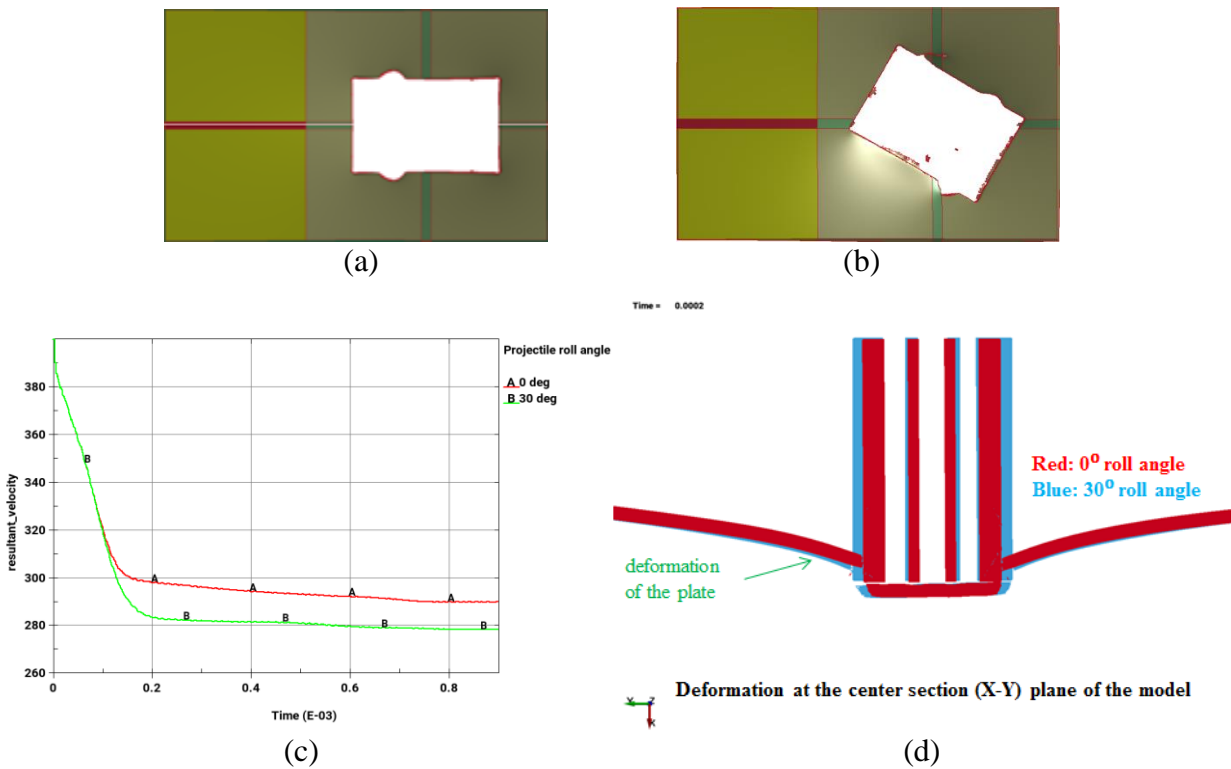
Figure 21. Comparison of two cases with 0º oblique angle: (a) penetration shape of the case with 0º roll angle; (b) penetration shape of the case with 30º roll angle; (c) velocity histories of the projectile (units: fps and second); and (d) overlapped snapshots at the center section plane of the model (at 0.2 msec)

7.1.1 Edge impact cases of the oblique angle variation series

Figure 22 shows the penetration shapes of the edge impact cases in the oblique angle variation series. The penetration shapes shown are half the total because the simulations used the half symmetric model. The penetration shape varies as the oblique angle varies. In 5º to 15º oblique angle variations, it can be seen that, at points, the failure deviated from the cutting edge of the projectile, as indicated by the red circle. The failure quickly returned to the cutting edge in the 5º oblique angle case, but in the 15º oblique angle case, it advanced away from the cutting edge to produce the wide petal or plug.

35
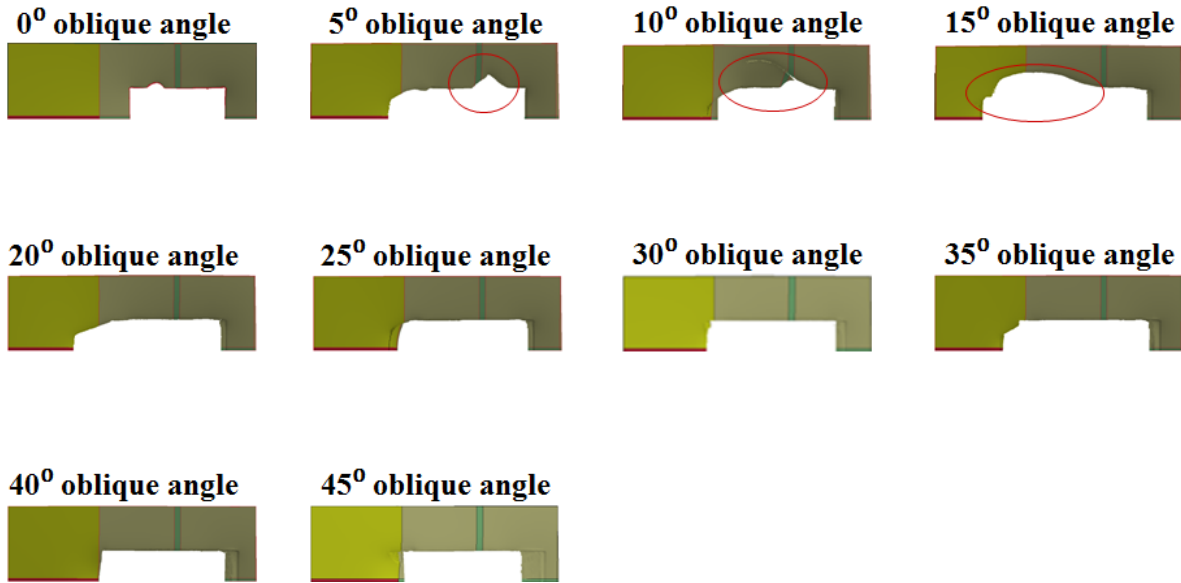
Figure 22. Penetration shapes of the edge impact cases in oblique angle variation series

The projectile velocity histories in the edge impact cases of the oblique angle variation series are shown in Figure 23, wherein green arrows indicate the failure initiation points. In general, the failure was initiated relatively later in the cases with lower oblique angles. In the higher oblique angle cases, the later part (after 0.4 msec) of the velocity curves are different from others, because the penetration behavior of the projectile changes. Figure 24 shows the snapshots of the ballistic impact simulations with 20° and 25° oblique angles at 0.5 msec. When the oblique angle is lower than 20°, the left-side face of the projectile does not contact the cut edge, as shown in Figure 24(a). When the oblique angle is higher than 25°, however, the left-side face of the projectile contacts with the cut edge, as shown in Figure 24(b). When the oblique angle increases, the velocity component of the projectile parallel to the plate surface increases the lateral movement of the projectile.

36
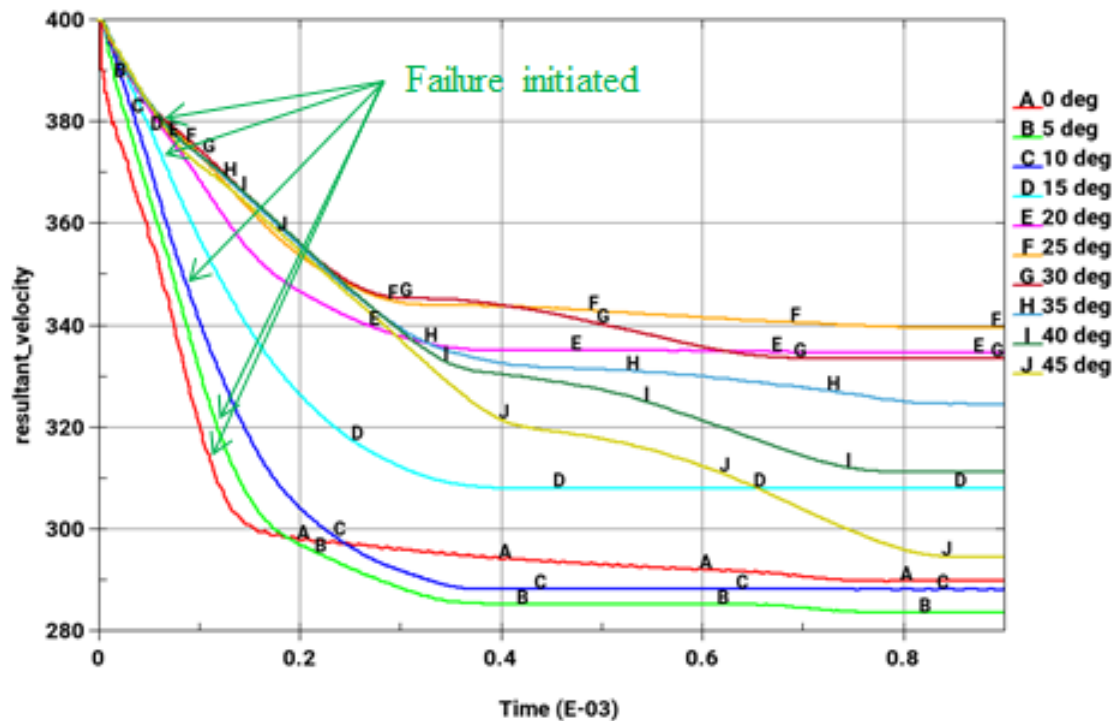
Figure 23. Velocity histories of the projectile in the edge impact cases of oblique angle variation series

(a)   (b)

Figure 24. Snapshots of two ballistic impact simulations at 0.5 msec: (a) 20º oblique angle and (b) 25º oblique angle

Figure 25 compares the baseline (0º oblique angle) with the lowest exit velocity case (5º oblique angle) and the highest exit velocity case (25º oblique angle). In the baseline case (red) with a 0º oblique angle, the contact area of the plate with the projectile was deforming at 0.1 msec, and then the failure process was already complete at 0.2 msec.

In the 5º oblique angle case (blue in Figure 25), the contact area of the plate is deforming at 0.1 msec, just as the baseline case. At 0.2 msec, the right contact edge of the plate has failed, but the left contact edge was still deforming, which causes more deformation in the plate than the baseline. Observing the velocity curve in Figure 23, both the baseline and the 5º oblique cases show failure initiation at similar times, but the 5º oblique angle case shows a longer failure propagation period

37

than the baseline. In the penetration shape in Figure 21, the area of the penetration hole in the 5° oblique case appears to be larger than the baseline. For these reasons, the exit velocity of the projectile in the 5° oblique angle case is lower than the baseline.

In the 25° oblique angle case (green in Figure 25), the right contact edge of the plate had already failed at 0.1 msec, and then the failure propagation process continued after 0.2 msec. The noticeable difference from the baseline is the reduced deformation of the plate because of the early failure initiation, as shown in the velocity curve in Figure 23, which is consistent with the exit velocity of the projectile in the 25° oblique angle case being higher than the baseline.

(a)   (b)
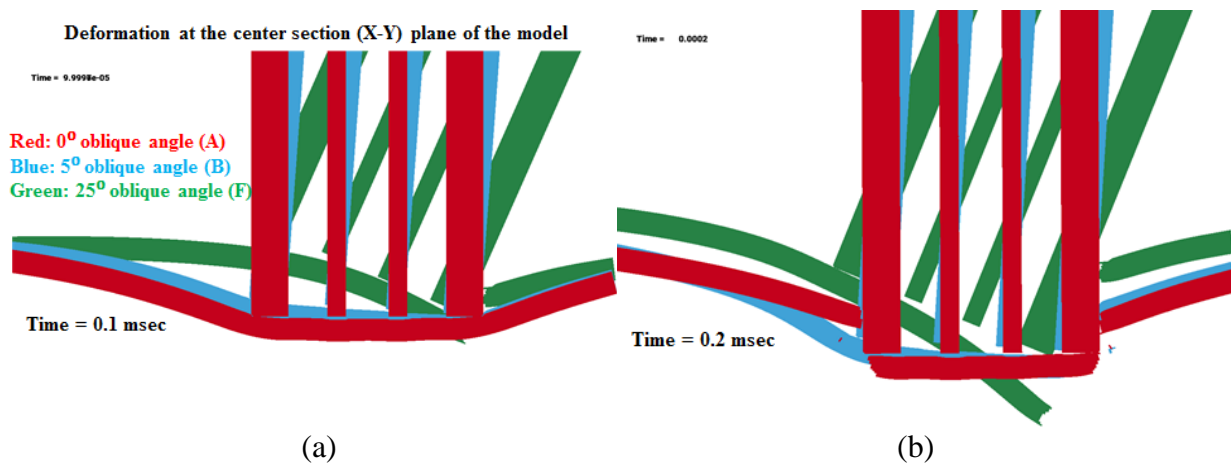
Figure 25. Comparison of the baseline with two edge impact cases with 5° and 25° oblique angles: (a) at 0.1 msec and (b) at 0.2 msec.

7.1.2 Corner impact cases of the oblique angle variation series

Figure 26 shows the penetration shapes of the corner impact cases in the oblique angle variation series. Similar to the edge impact cases described above, the penetration shape varies as the oblique angle varies. In the 5° to 20° oblique angle variations, the failure deviated from the cutting edge of the contact area, and a larger penetration hole was created.
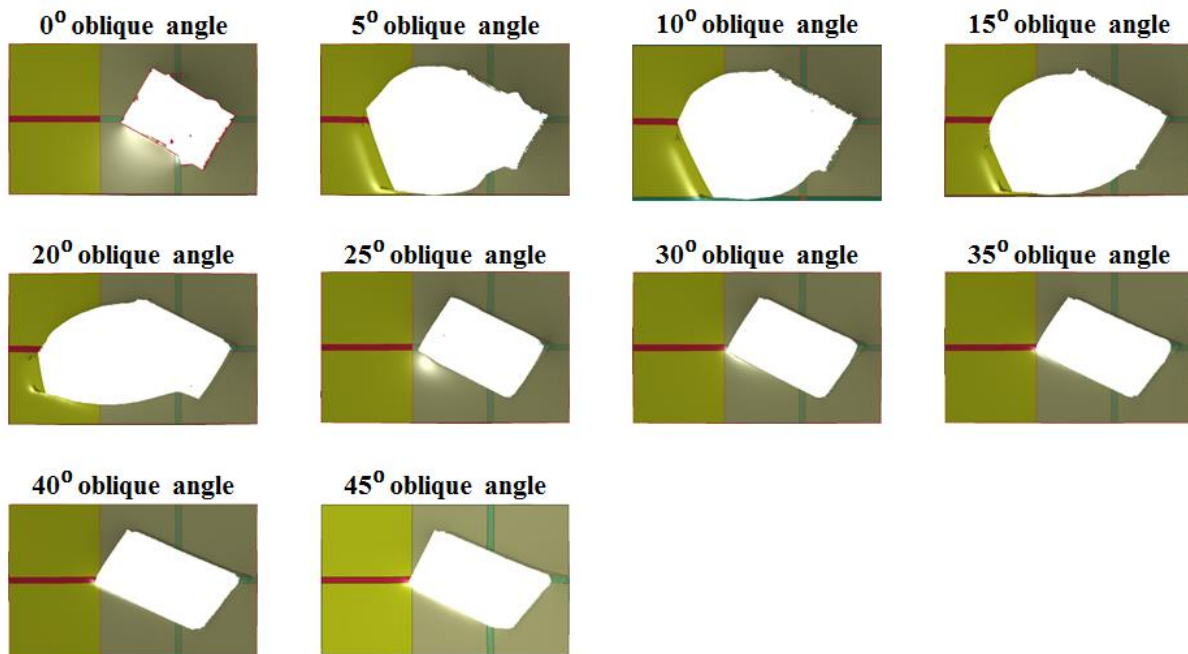
Figure 26. Penetration shapes of the corner impact cases in oblique angle variation series

Figure 27 shows the projectile velocity histories in the corner impact cases of the oblique angle variation series. The failure initiation points in 0º, 5º, and 25º oblique angle cases are indicated by the arrows in Figure 27. Similar to the edge impact cases, the failure was initiated relatively later in the cases with lower oblique angles. In the higher oblique angle cases, the later part (after 0.4 msec) of the velocity curves are different from others, because the penetration behavior of the projectile changes, which is similar to the edge impact cases. When the oblique angle is lower than 20º, the left-side face of the projectile does not contact with the cut edge. Instead, the large petal was developed. When the oblique angle is higher than 25º, however, the left-side face of the projectile contacts with the cut edge.
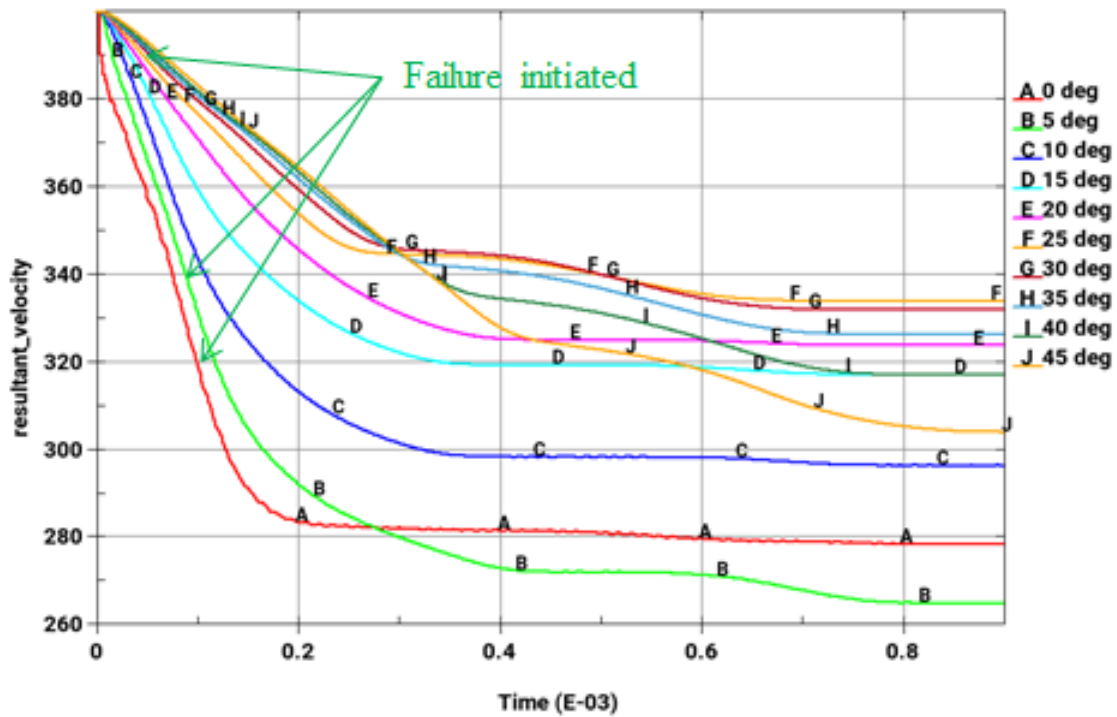
Figure 27. Velocity histories of the projectile in the corner impact cases of oblique angle variation series

Figure 28 compares the baseline (0° oblique angle) with the lowest exit velocity case (5° oblique angle) and the highest exit velocity case (25° oblique angle). These penetration processes in the corner impact cases shown in Figure 28 are similar to those in the edge impact cases, shown in Figure 25. The slight difference can be seen in the 5° oblique angle case (blue). At 0.2 msec in Figure 28(b), failure was initiated at the right contact corner of the plate and propagated along the cutting edge. However, the failure propagation deviated away from the cutting edge, making the penetration hole larger than the baseline, as shown in Figure 26. The developed petal broke away at 0.7 msec, as shown in Figure 28(c). Therefore, the exit velocity in the 5° oblique angle corner impact case is lower than one in the edge impact case, as shown in Figure 20.

(a)   (b)

(c)
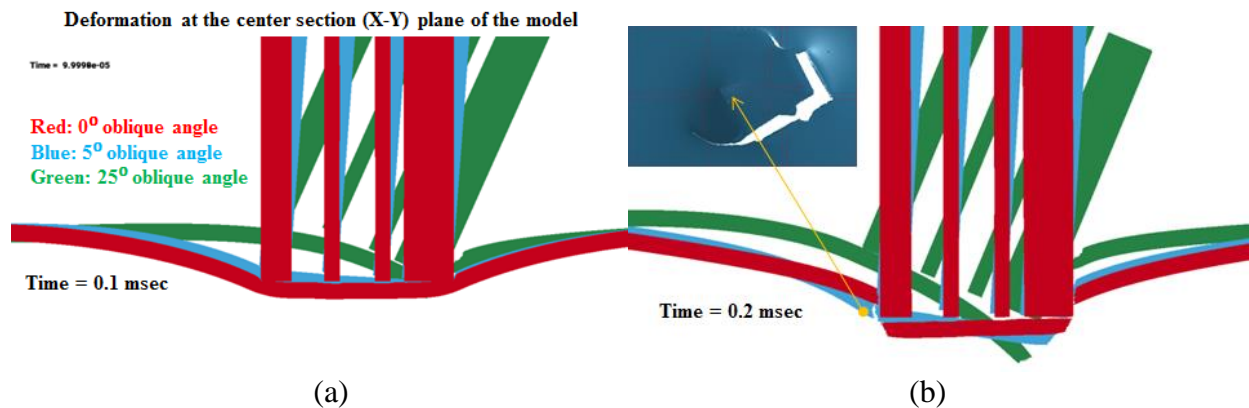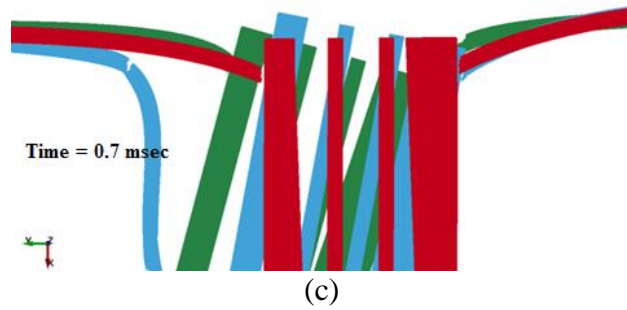
Figure 28. Comparison of the baseline with two corner impact cases with 5º and 25º oblique angles: (a) at 0.1 msec, (b) at 0.2 msec, and (c) at 0.7 msec.

7.2 Attitude angle variation

The attitude angle study was conducted to assess the sensitivity of projectile angular orientation with respect to its flight path. Because of the test setup configuration, only target plate tilt and projectile roll had to be varied to accomplish all combinations of attitude angle desired. In the tests shown in Table 1, the roll, pitch, and yaw angles of the projectile were changed by as much as 15º to accomplish the desired conditions.

In order to determine the sensitivity of exit velocity to small changes in projectile attitude angle variation, four series of ballistic impact simulations were conducted. The face impact case, #6.1.1, was selected as a baseline, and four small attitude angle variation series were considered:

- Roll angle variation: (1,0,0), (2,0,0) and (3,0,0)
- Pitch angle variation: (0,-3,0), (0,-2,0), (0,-1,0), (0,1,0), (0,2,0) and (0,3,0)
- Yaw angle variation: (0,0,1), (0,0,2) and (0,0,3)
- Pitch and yaw angle variation: (0,-3,3), (0,-2,2), (0,-1,1), (0,1,1), (0,2,2) and (0,3,3)

The numbers shown in parentheses identify roll angle, pitch angle, and yaw angle in degrees. Figure 29 shows the small angle variations for one orientation condition. In all ballistic simulations for this series, the oblique angle was set to 0º (face impact), as indicated by the blue arrow in Figure 29. Figure 15 show that the exit velocity of the projectile is sensitive to the oblique angle when the impact velocity is high enough to the ballistic limit velocity. However, near the ballistic limit velocity, the exit velocity is more sensitive to the attitude angle of the projectile than the oblique angle. The estimated ballistic limit velocity of #6.1.1 in the simulation is 318 fps. The impact velocity of the projectile in all of the attitude angle variation simulations was set to 325 fps (just above the ballistic limit) to investigate the effects of attitude angle variation effects on both the exit velocity and ballistic limit. Figure 30 shows the face views of the ballistic impact setups for all of the highest attitude angles relative to the baseline.
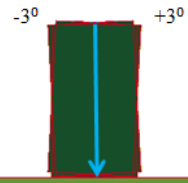
Figure 29. Overlap of ballistic impact setups of the attitude angle variation series (blue arrow indicates the projectile flight direction)
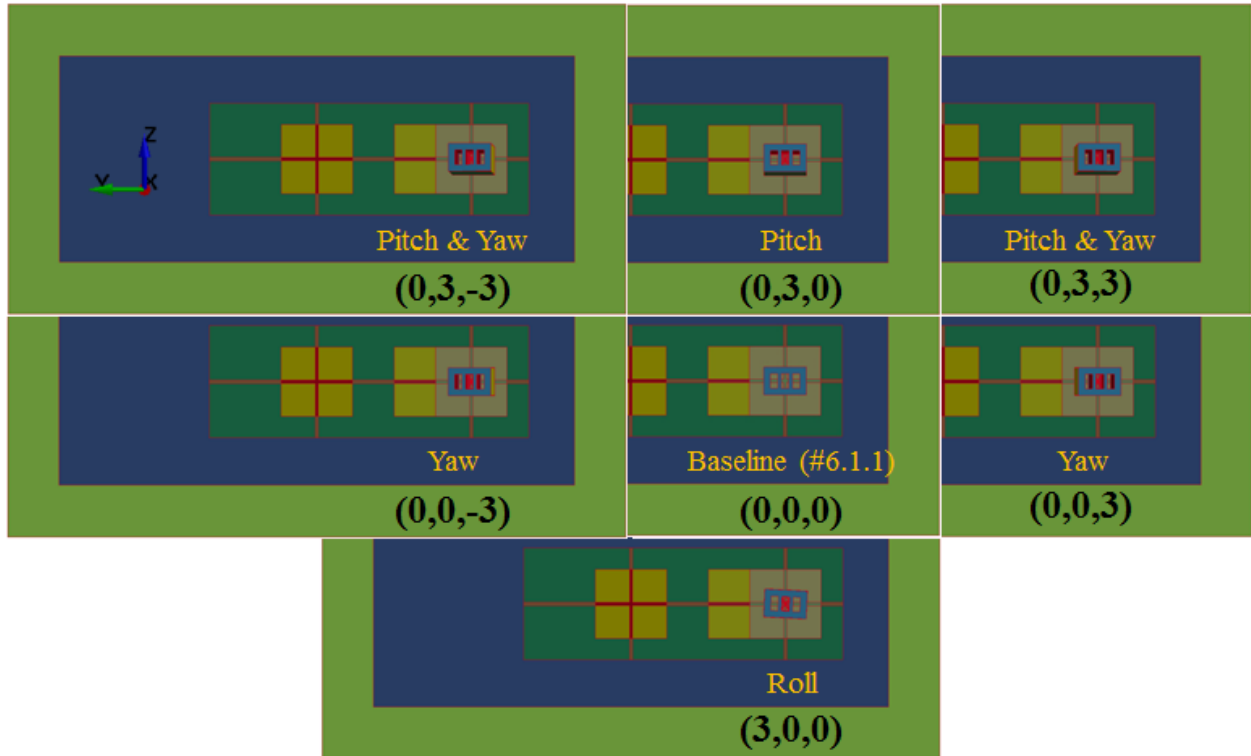
Figure 30. Top views of ballistic impact setups of the attitude angle variation series with roll angle, pitch angle, yaw angle in degrees

Figure 31 summarizes the exit velocities of the projectile for all the simulations in the attitude angle variation series. In this figure, the baseline condition is shown in black. The cases shown in red indicate that the exit velocities are lower than the baseline, and cases in blue identify the cases with exit velocities greater than the baseline. This illustrates that there can be large variations in the exit velocity with attitude angle variation. For this study, the variation relative to baseline is 86 fps, from 75 fps (-37%) to 161 fps (34%). The exit velocity is increased in the pitch angle variation, but mostly decreased in other variations.

Figure 31. Exit velocities of the projectile in attitude angle variation series (red or blue indicate the decrease or increase of the exit velocity from the baseline, respectively)

Figure 32 shows the penetration shapes in the target plates for all the attitude angle variation simulations conducted. It appears that the penetration shapes differ from the baseline with changes in attitude angle. Noticeably, the penetration holes are much larger (greater energy absorbed) in the cases with both pitch and yaw angle variations than conditions with just pitch or yaw, which explains the large decreases in exit velocity shown in Figure 31.

43
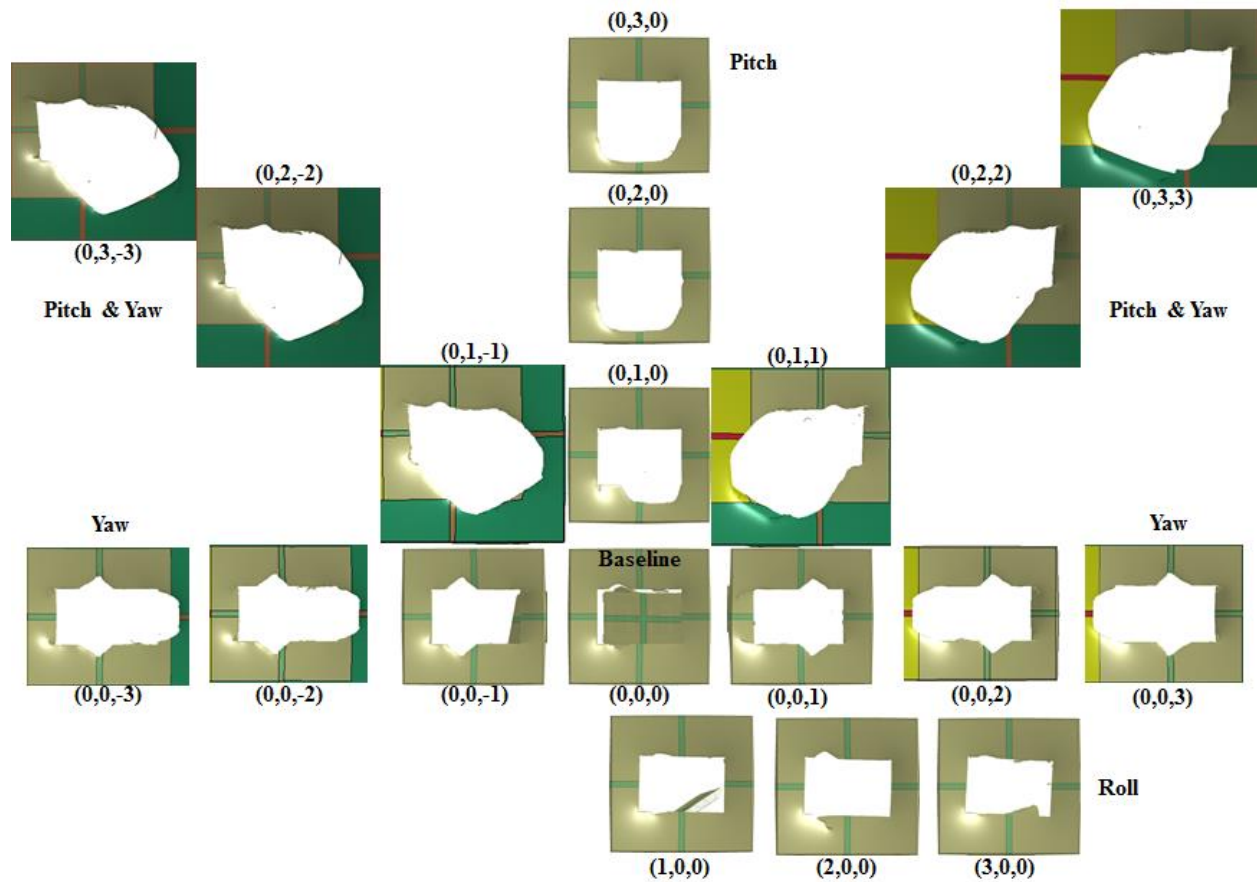
Figure 32. Penetration shapes in attitude angle variation series

Figure 33 shows an estimated range of ballistic limit velocity with attitude angle variation. The ballistic limit velocities for the cases shown were estimated by assuming that the exit velocity at the 400 fps impact velocity is the same regardless of the attitude angle variation. This is a reasonable assumption because Figure 15 showed that the exit velocity is not sensitive to attitude angle at the 400 fps impact velocity. (The selected velocity was somewhat arbitrary and was within the range of interest.) The maximum and minimum fit curves were approximated by using the exit velocity points (orange small circles) in the attitude angle variation series. The ballistic limit velocity for baseline #6.1.1 was estimated as 318 fps, and its variation range in the attitude angle variation series, as based on the baseline, is estimated to be 16 fps, from 307 fps (-3.5%) to 323 fps (1.6%). This is relatively small compared to the exit velocity variation range (86 fps).
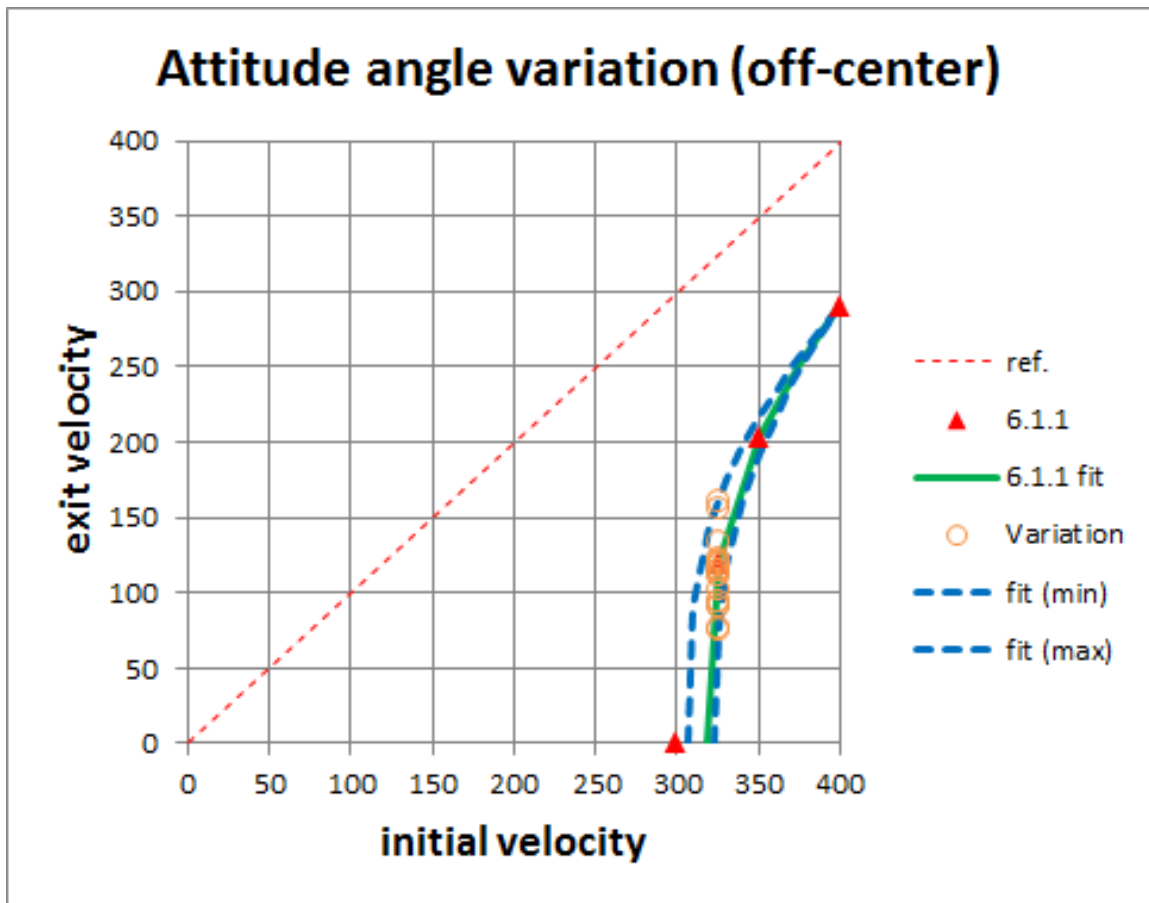
Figure 33. Estimated range of ballistic limit velocity in attitude angle variation series

Figure 34 through Figure 37 compare the baseline small face impact condition (#6.1.1) with the attitude angle variation series. In these figures, the velocity histories of the projectile are shown first, then the cross-section plane views of the baseline and the variation are compared.

In the roll angle variation series, the projectile exit velocity decreases as the roll angle varies, as shown in Figure 31 and Figure 34(a). The variation range based on the baseline is small in the 1° and 3° roll angle variation cases, but it is large in the 2° case. Figure 34(b) compares the baseline with the 2° case. The difference between the two cases is the deformation of the plate; the deformation in the 2° case (blue) is larger than the baseline (red). The penetration shapes in the roll angle variation cases are very similar to the baseline, as shown in Figure 32.

(a)   (b)
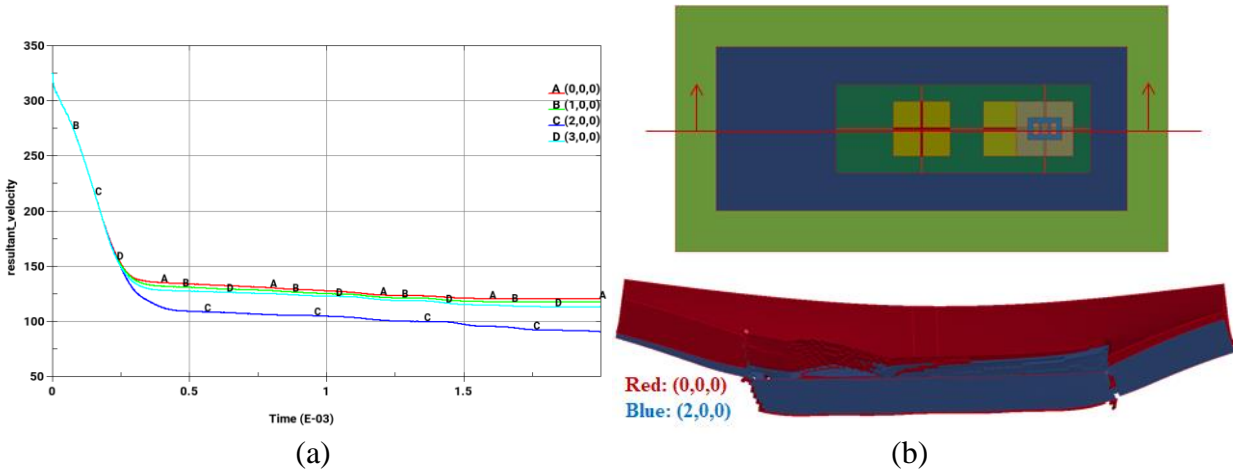
**Figure 34. Comparison of the baseline with the others of the roll angle variation series:
(a) projectile velocity histories and (b) cross-section plane views at 0.3 msec.**

In the pitch angle variation series, the exit velocity of the projectile increases as the pitch angle varies, as shown in Figure 31 and Figure 35(a). The variation range from the baseline goes to as large as 34% in the 3° roll angle variation case. In Figure 35(b), the pitch angle variation (blue) initiated the early left edge failure and caused less deformation in the plate than the baseline (red), which developed the larger penetration hole in the plate seen in Figure 32.

46
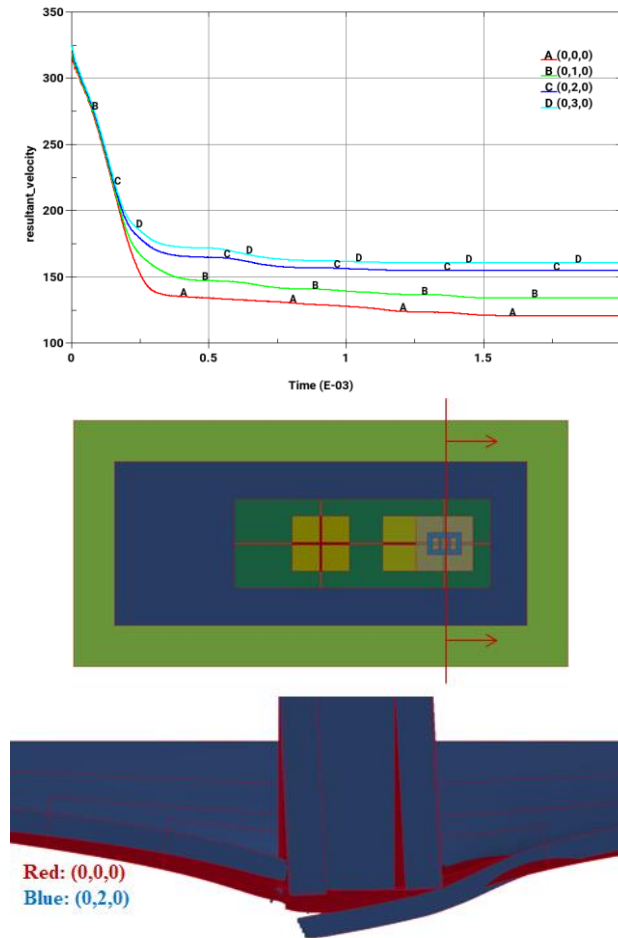
Figure 35. Comparison of the baseline with the others of the pitch angle variation series: (a) projectile velocity histories and (b) cross-section plane views at 0.3 msec

In the yaw angle variation series, the exit velocity of the projectile varies minimally as the yaw angle varies, as shown in Figure 31 and Figure 36(a). The yaw angle variation initiated the early right edge failure and developed the larger penetration hole in the plate, as shown in Figure 32 and Figure 36(b), which can be confirmed by the changes of the velocity curves in Figure 36(a). However, the plate deformations between the baseline and the 2° yaw angle variation case are comparable, as shown in Figure 36(b), which makes the exit velocity variation minimal.
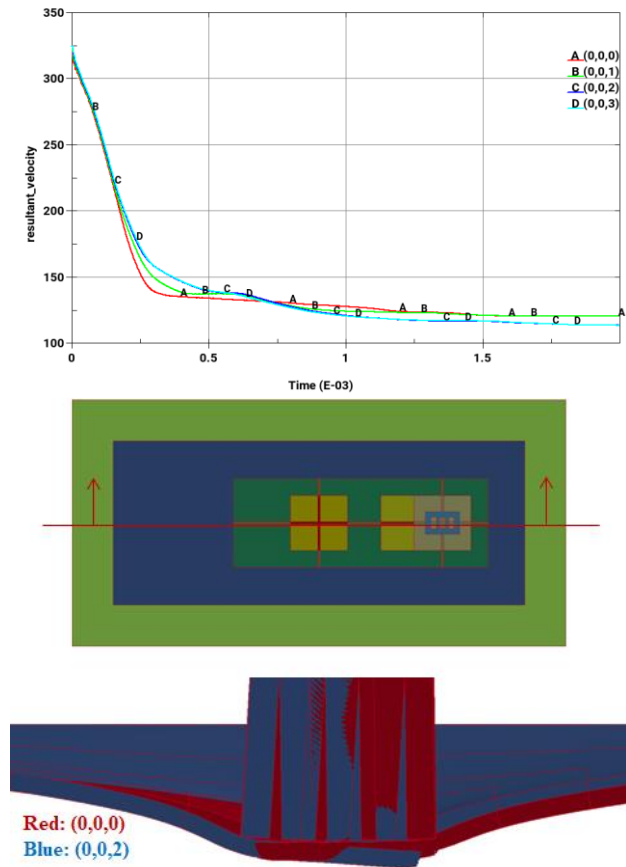
Figure 36. Comparison of the baseline with the others of the yaw angle variation series: (a) projectile velocity histories and (b) cross-section plane views at 0.3 msec.

In both pitch and yaw angle variation series, the exit velocity of the projectile decreases as both the pitch and yaw angles vary, as shown in Figure 31 and Figure 37(a). Similarly, both the pitch and yaw angle variations initiated the early right edge failure, and developed the very large penetration hole in the plate seen in Figure 32 and Figure 37(b). The smaller pitch and yaw angle variation caused the larger plate deformation, which makes the exit velocity smaller.
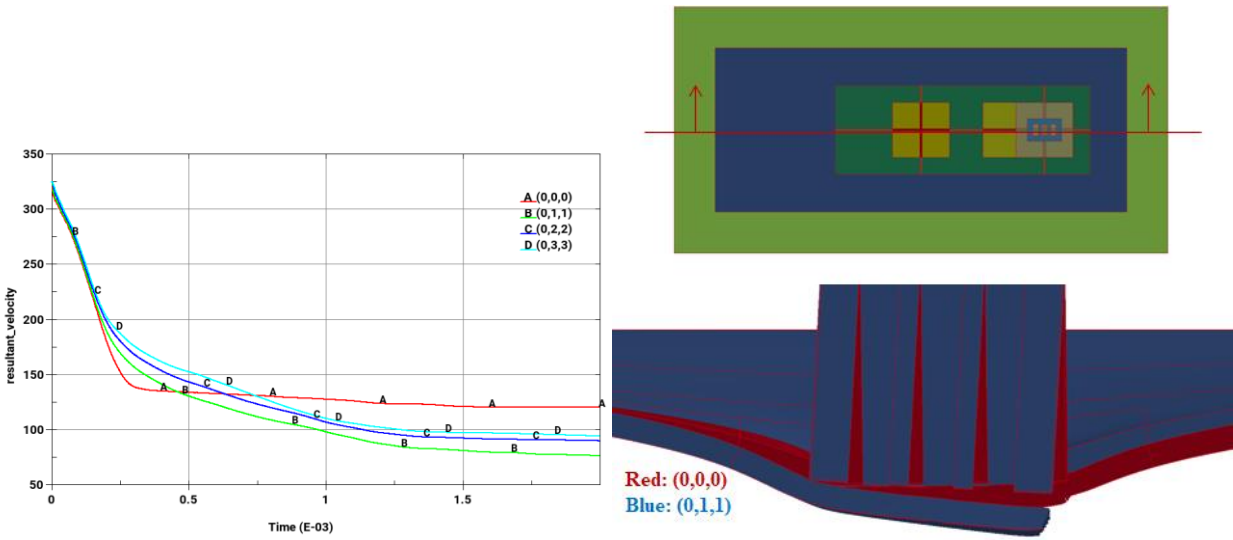
Figure 37. Comparison of the baseline with the others of the pitch and yaw angle variation series: (a) projectile velocity histories and (b) cross-section plane views at 0.3 msec.

It should be noted that the simulation results of the angle variation cases have not been confirmed with test results, and that some simulation results differ from the expected trends of ballistic impact tests. In general, it was expected that any angle variation in the face impact configuration tended to increase the projectile exit velocity [12]. However, the simulation results showed that there were exit velocity decreases in some angle variation cases, such that the exit velocity was decreasing when the oblique angle was varied to 5° initially and the pitch and yaw angles were varied from 1° to 3°.

At this point, it is not known how precisely the simulations are able to describe all the physical penetration processes that occurred in ballistic impact tests with small angle variations. So, these simulation results presented here need to be interpreted carefully. At a minimum, the simulation results show that the projectile exit velocity could be very sensitive to small variations of the oblique and attitude angles in the face impact configuration of the ballistic impact. This could be the cause of the small differences between tests and simulations reported in Section 6. The simulation results reinforce what is demonstrated by the testing; that the physical processes of ballistic impact are both complicated and sensitive.

8. CONCLUSIONS

In this research work, a series of ballistic impact simulations was conducted using LS-DYNA to simulate ballistic tests conducted at NASA to provide data for validating *MAT_224 for Aluminum 2024. In the ballistic impact test setup, a rectangular parallelepiped-shaped Inconel 718 projectile with sharp corners and edges, impacts an Aluminum 2024 panel with various oblique and attitude angles, impact velocities, and impact points. The *MAT_224 material model for Aluminum 2024 (Version 2.0) was used for the Aluminum target plate. No correlation modifications were made to this material input dataset as part of this effort. The simulations show good agreement with NASA ballistic impact experiments, thereby validating the Aluminum 2024 *MAT_224 model and illustrating the model predictive fidelity under challenging impact conditions.

The simulation sensitivity study concluded that:

- The element size should be within the range of the regularization table (LCI) in *MAT_224.
- Reduced integration for solid elements reduces accuracy (~7%) but provides an acceptable means to reduce computing runtime.
- The ballistic impact simulations are not sensitive to HPC machine types, provided element size is within regularization limits.

The ballistic impact tests were simulated to validate the new *MAT_224 for Aluminum 2024 and to evaluate its predictability. The results demonstrate that:

- Overall, the simulations correlate well with tests with regard to projectile residual velocities, failure shapes of a target plate, and projectile penetration behavior.
- In face impact cases, the penetration shapes between tests and simulation differed, specifically in the post-rupture petaling. The differences could be caused by sensitivity to test attitude angle variations.
- In cases with a 60º projectile roll angle, the projectile exit velocities in the simulations are lower than those in the tests. This could be caused by the difference in mesh patterns of the projectile and the target at the impact site.
- The exit velocity of the projectile is more sensitive to the oblique angle than the projectile roll angle, when the impact velocity is high enough above the ballistic limit velocity. Near the ballistic limit, exit velocities are sensitive to both the projectile roll angle and impact configurations.
- The simulations predicted the ballistic limit velocities well within the test velocity variation.

The effects of the variations of oblique and attitude angles to the ballistic impact simulation show that:

- For impact simulations with a 400 fps initial velocity, the projectile exit velocity varies with obliquity angle as the target plate tilt angle (oblique angle) is changed from 0º to 45º (studied in 5º tilt intervals). The projectile exit velocity was lowest at 5º obliquity and highest at 25º.

- Attitude sensitivity was investigated for a projectile initial velocity of 325 fps (near the ballistic limit) and four attitude angle conditions (roll, pitch, yaw, and the combination of pitch and yaw). Attitude angle was varied from 0º to 3º in 1º increments. The results show that there is a large variation in the exit velocity with attitude angle variation. However, the variation range of the ballistic limit velocities is relatively small, compared to the influence on exit velocities above the ballistic limit.

9. REFERENCES

[1] W. Emmerling, D. Altobelli, K. Carney, and M. Pereira, "Development of a new metal material model in LS-DYNA part 1: FAA, NASA, and industry collaboration background," Final Report, DOT/FAA/TC-13/25, P1, April 2014.

[2] M. Buyuk, "Development of a new metal material model in LS-DYNA part 2: Development of a tabulated thermo-viscoplastic material model with regularized failure for dynamic ductile failure prediction of structures under impact loading," Final Report, DOT/FAA/TC-13/25, P2, July 2014.

[3] Livermore Software Technology Corporation, *LS_DYNA Keyword User's Manual*, Volume I and II, Version R10.0, Livermore, California, 2017.

[4] J.D. Seidt, "Development of a new metal material model in LS-DYNA part 3: Plastic deformation and ductile fracture of 2024 aluminum under various loading conditions," Final Report, DOT/FAA/TC-13/25, P3, April 2014.

[5] J. Pereira, D. Revilock, B. A. Lerch and C. Ruggeri, "Impact Testing of Aluminum 2024 and Titanium 6Al-4V for Material Model Development," 2013.

[6] C.K. Park, K. Carney, P. Du Bois, D. Cordasco, and C.D. Kan "Aluminum 2024-T351 input parameters for *MAT_224 in LS-DYNA," Final Report, DOT/FAA/TC-19/41 P1 .

[7] C. Ruggeri, D. Revilock, M. Pereira, W. Emmerling, and G. Queitzsch, "Impact and penetration of thin Aluminum 2024 flat panels at oblique angles of incidence," NASA/TM—2015-218484, DOT/FAA/TC-15/7.

[8] J. Smith, "Full-Field Measurement of the Taylor-Quinney Coefficient in Tension Tests of Ti-6Al-4V, Aluminum 2024-T351, and Inconel 718 at Various Strain Rates," PhD Dissertation, Ohio State University, 2019.

[9] S. Dolci, K. Carney, L. Wang, C.D. Kan, and P. Du Bois, "Incorporation of Inconel-718 material test data into material model input parameters for *MAT_224," 14th International LS-DYNA Users Conference, Dearborn MI, June 2016.

[10] R.F. Recht, and T.W. Ipson, "Ballistic perforation dynamics," *Journal of Applied Mechanics*, Volume 30, Pages 384–390, 1963.

[11] T. Børvik, O.S. Hopperstad, and K.O. Pedersen, "Quasi-brittle fracture during structural impact of AA7075-T651 aluminum plates," *International Journal of Impact Engineering*, Volume 37, Issue 5, Pages 537–551, 2010.

[12] M. Pereira, Personal Communication, May 2019.

APPENDIX A. Simulations of NASA ballistic impact tests

Table A-1. Simulations of NASA ballistic impact tests

Test Setup No.	Impact Location of Panel	Oblique Angle (deg) Panel Tilt Angle	Attitude Angle (deg) Proj. Roll Angle	Proj. Pitch Angle	Proj. Yaw Angle	Impact Velocity (fps)	Exit Velocity (fps)	Curve Fitting Parameters in Eq. (6.1) Ballistic Limit Velocity (fps)	a	b
6.1.1		0	0			300	0.0	318	0.91	3.06
						325	120.0			
						350	204.0			
						400	290.0			
6.2.1			0			225	0.0	234	1.00	1.66
						250	64.7			
						300	151.0			
						400	295.0			
6.2.2			30			200	0.0	205	1.00	1.54
						225	63.7			
						250	103.0			
						300	174.0			
		45				400	304.0			
6.2.3			60			200	0.0	220	1.00	1.66
						225	33.8			
						250	85.3			
						300	175.0			
						400	304.0			
6.2.4	Center		90	0	0	250	0.0	272	0.92	2.30
						275	51.0			
						300	139.0			
						350	222.0			
						400	293.0			
6.2.5			0			175	0.0	198	1.00	1.78
						200	21.0			
						250	135.0			
						300	208.0			
						400	334.0			
6.2.6			30			175	0.0	193	0.96	1.94
						200	48.3			
						250	148.0			
		30				300	217.0			
						400	332.0			
6.2.7			60			175	0.0	186	0.99	1.70
						200	56.8			
						250	144.0			
						400	329.0			
6.2.8			90			200	0.0	211	0.97	1.98
						225	75.7			
						250	123.0			
						300	211.0			
						400	327.0			

Table A-2. Simulations of NASA ballistic impact tests (continued)

Test Setup No.	Impact Location of Panel	Oblique Angle (deg) Panel Tilt Angle	Attitude Angle (deg) Proj. Roll Angle	Attitude Angle (deg) Proj. Pitch Angle	Attitude Angle (deg) Proj. Yaw Angle	Impact Velocity (fps)	Exit Velocity (fps)	Curve Fitting Parameters in Eq. (6.1) Ballistic Limit Velocity (fps)	a	b
7.1.1	Off-Center	0	0	0	0	300	0.0	316	0.90	3.10
						325	132.0			
						350	207.0			
						400	291.0			
7.1.2			60			300	0.0	324	0.91	2.98
						325	57.2			
						350	192.0			
						400	279.0			

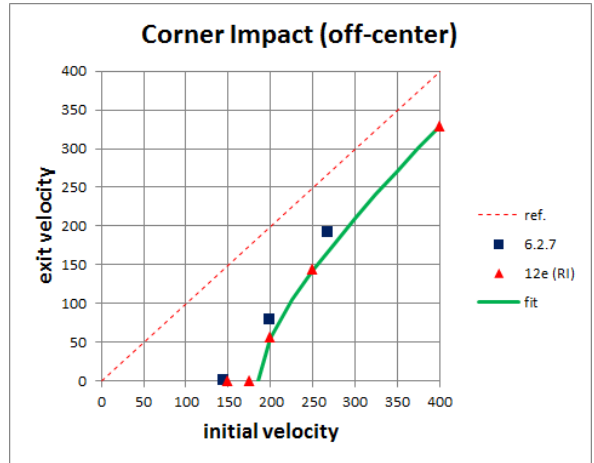# APPENDIX B. Results of NASA ballistic impact simulations
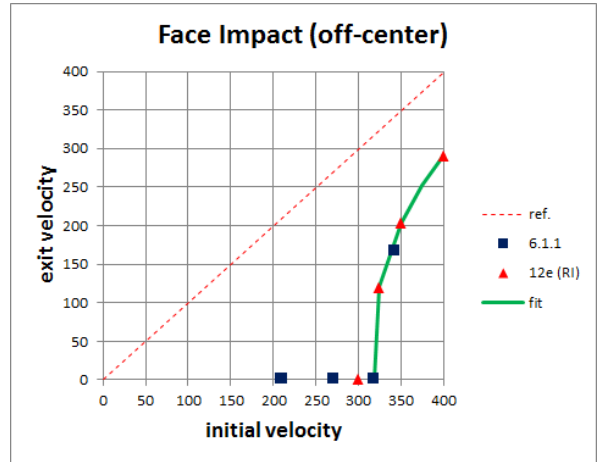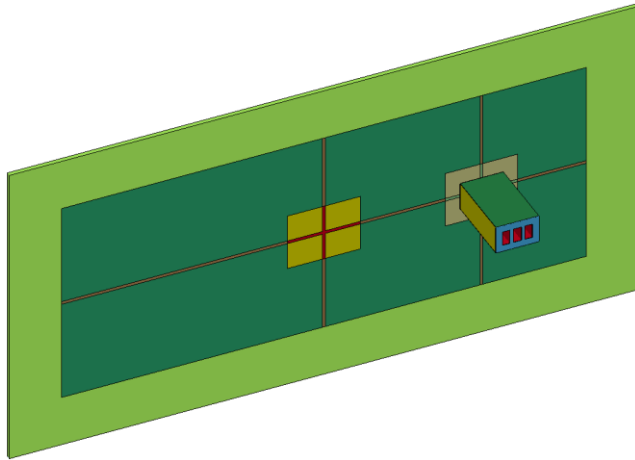
(a)

(b)

(c)
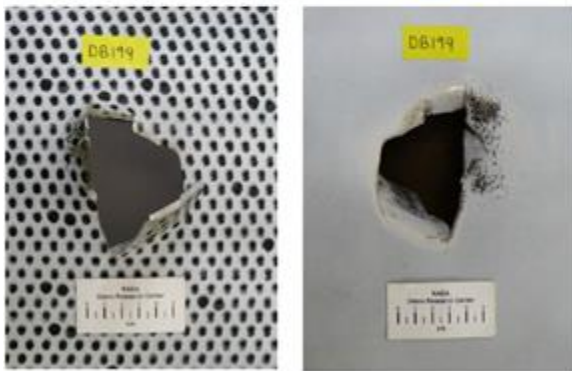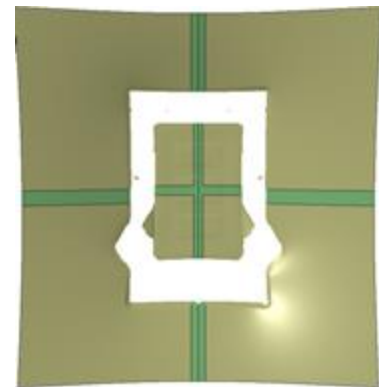
(d)

Figure B-1. Simulation results of test setup #6.1.1: (a) impact setup; (b) exit velocities of the projectile; (c) plate deformation in tests [7]; and (d) plate deformation in simulations
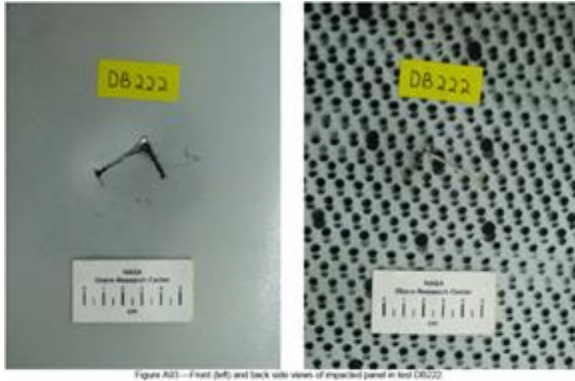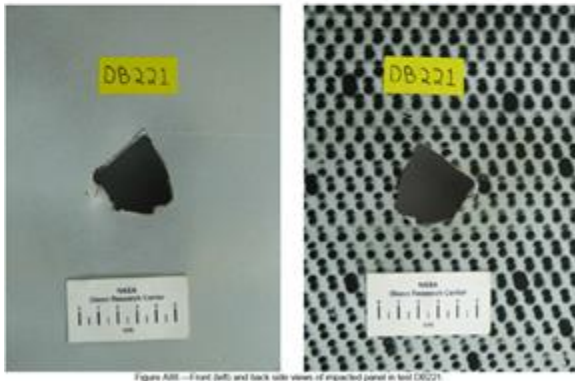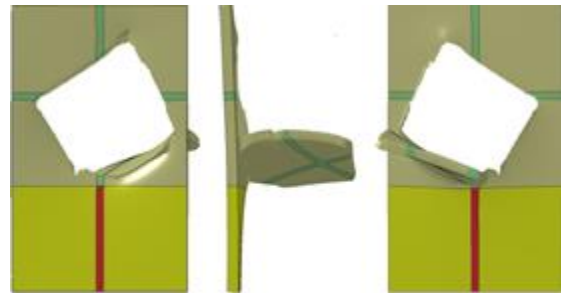
(a)

(b)
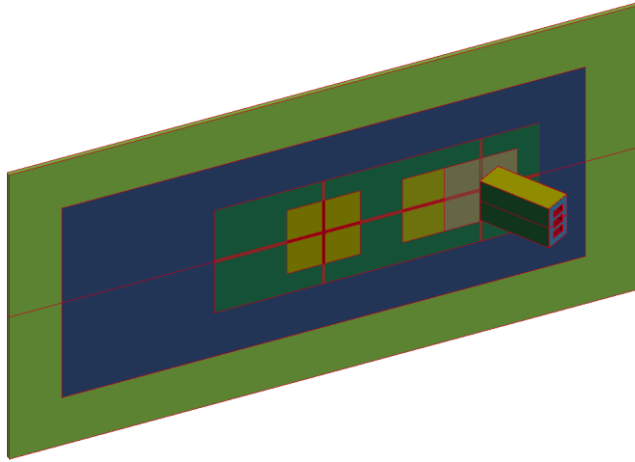
(c)
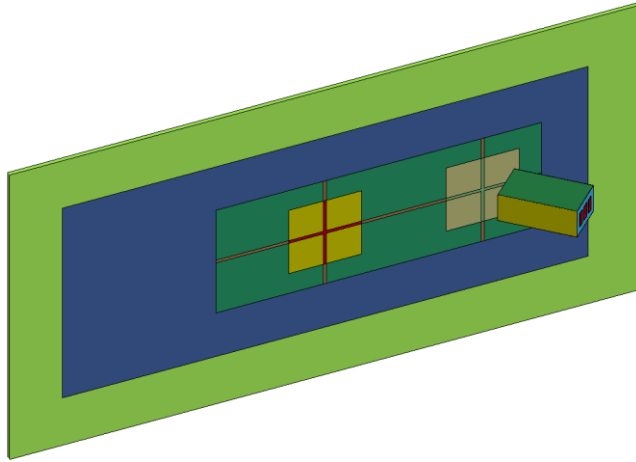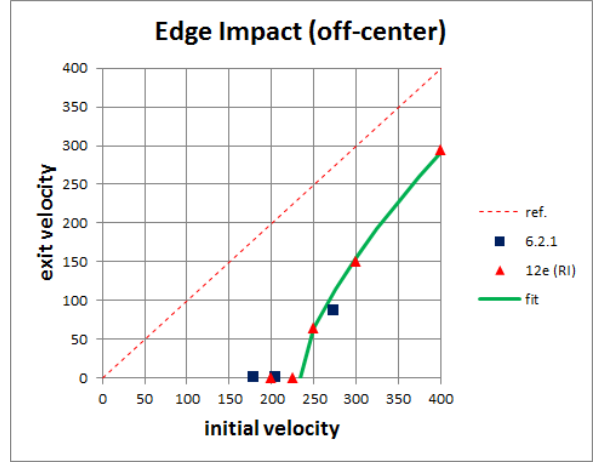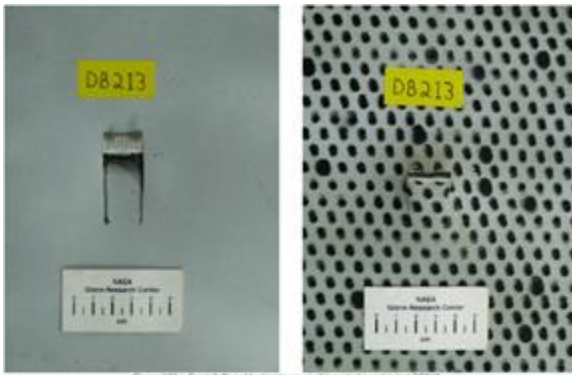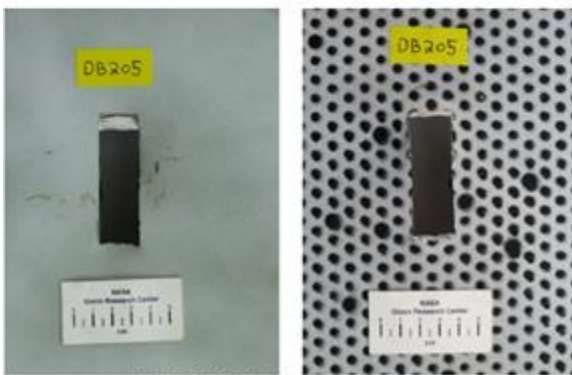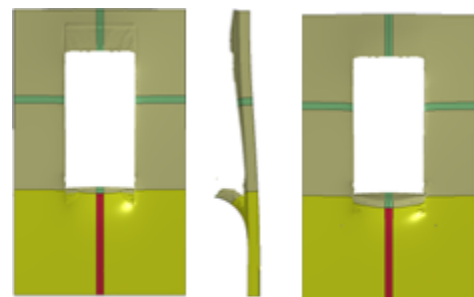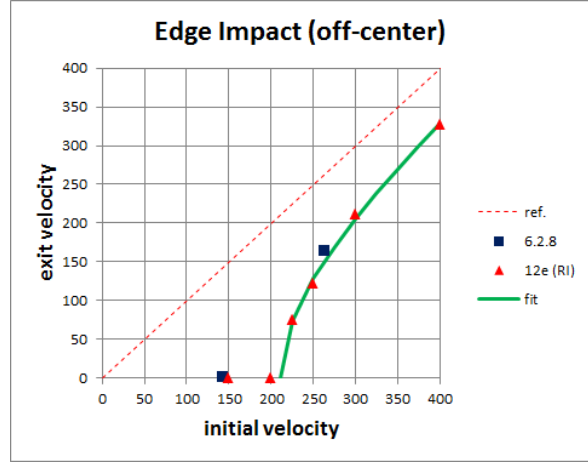
(d)

Figure B-2. Simulation results of test setup #6.2.1: (a) impact setup; (b) exit velocities of the projectile; (c) plate deformation in tests [7]; and (d) plate deformation in simulations

(a)

(b)

(c)
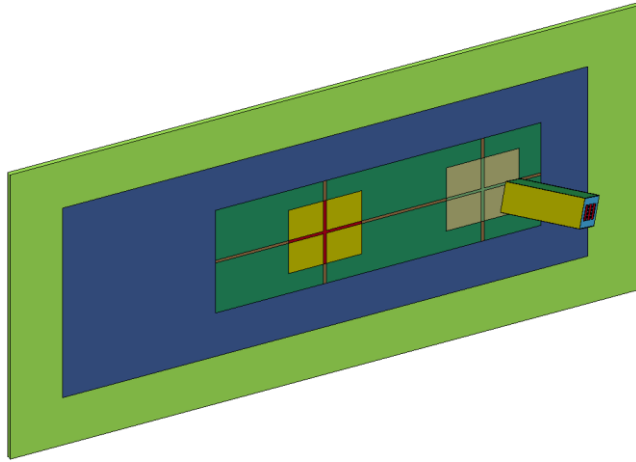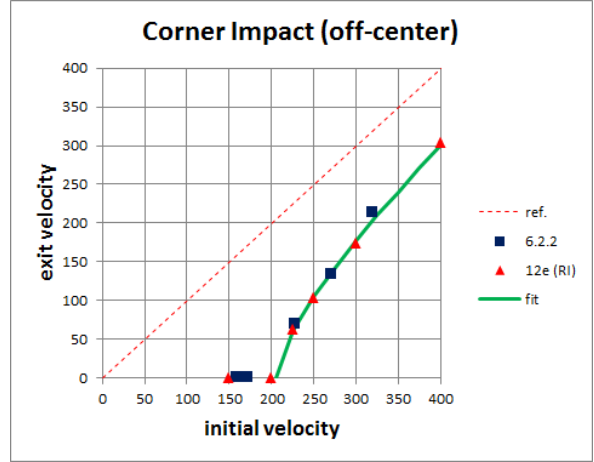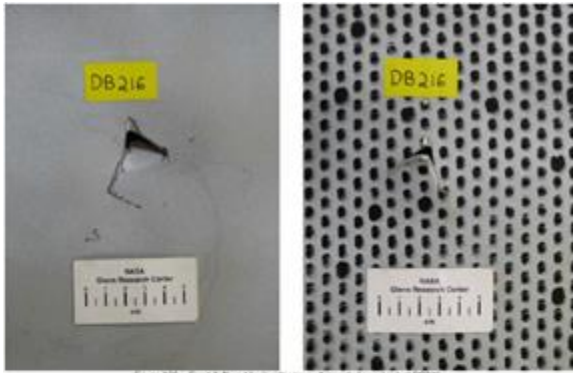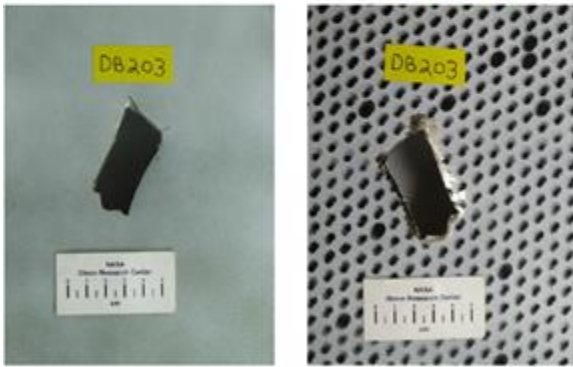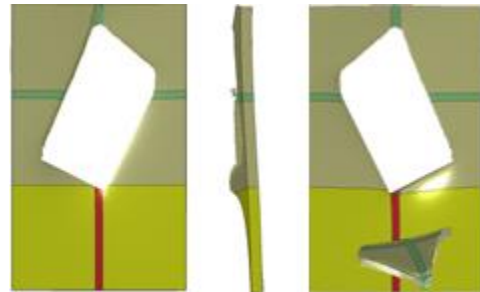
(d)

Figure B-3. Simulation results of test setup #6.2.2: (a) impact setup; (b) exit velocities of the projectile; (c) plate deformation in tests [7]; and (d) plate deformation in simulations
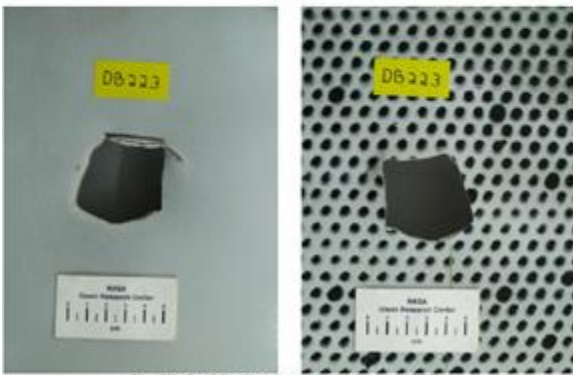
B-3

(a)

(b)

(c)
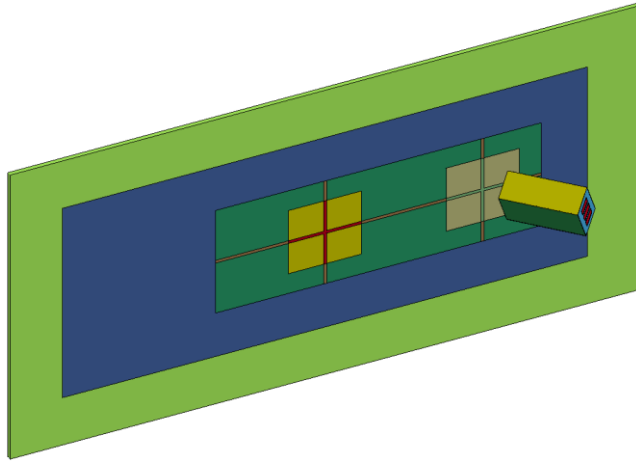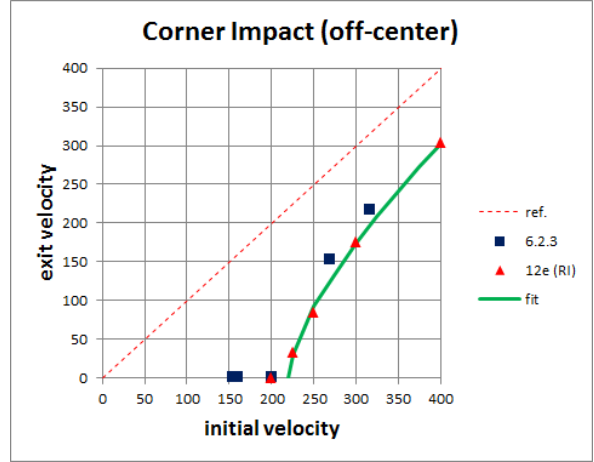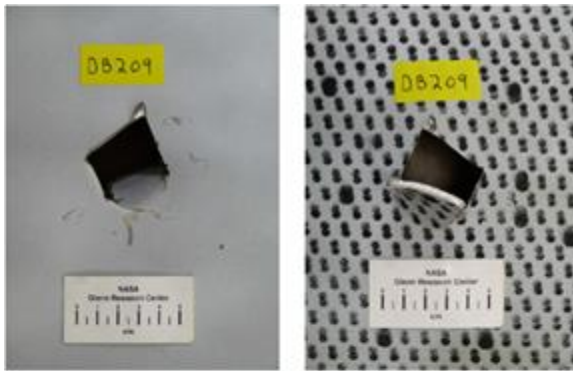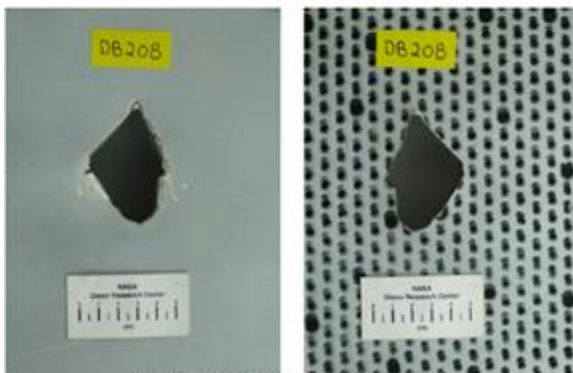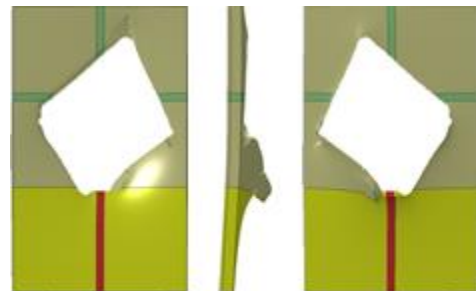
(d)

Figure B-4. Simulation results of test setup #6.2.3: (a) impact setup; (b) exit velocities of the projectile; (c) plate deformation in tests [7]; and (d) plate deformation in simulations
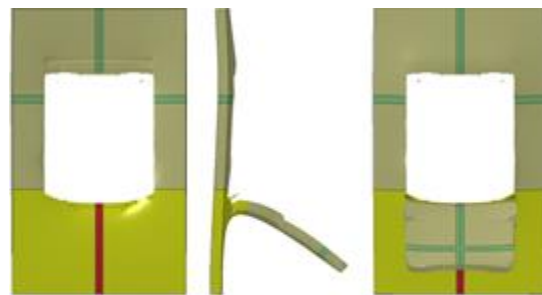
(a)

(b)

(c)
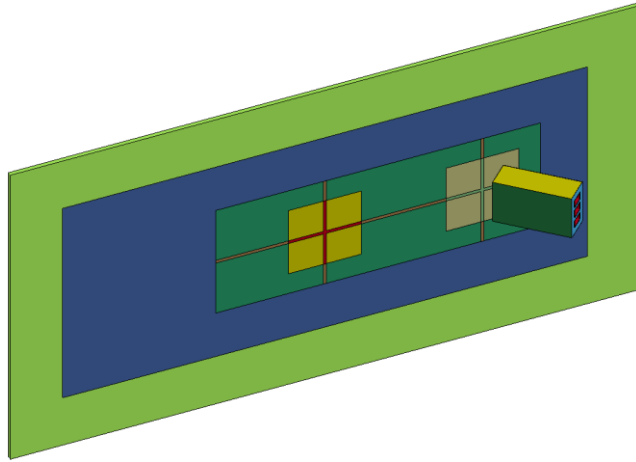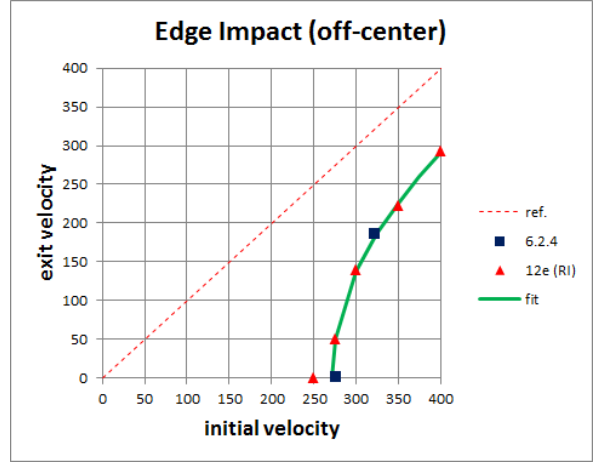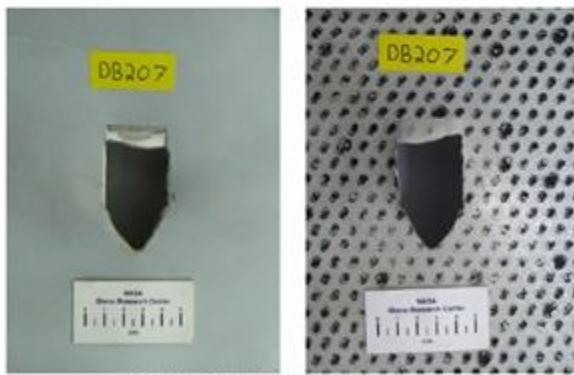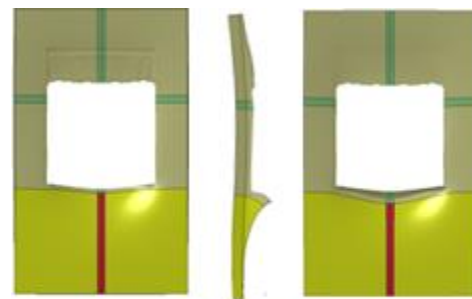
(d)

Figure B-5. Simulation results of test setup #6.2.4: (a) impact setup; (b) exit velocities of the projectile; (c) plate deformation in tests [7]; and (d) plate deformation in simulations
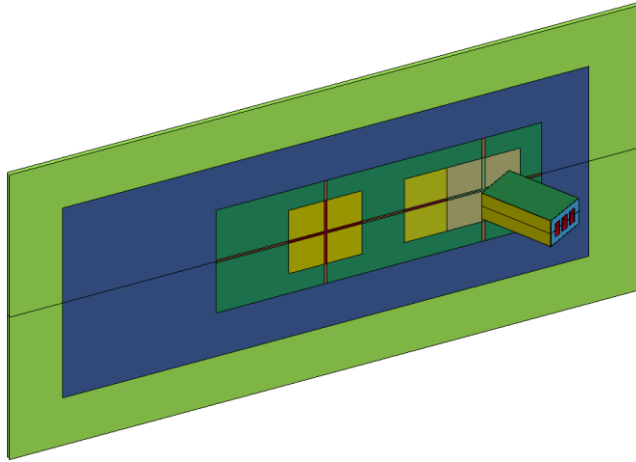
(a)
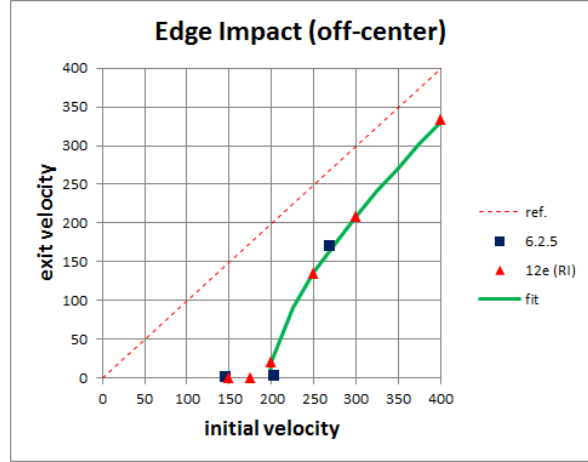
(b)
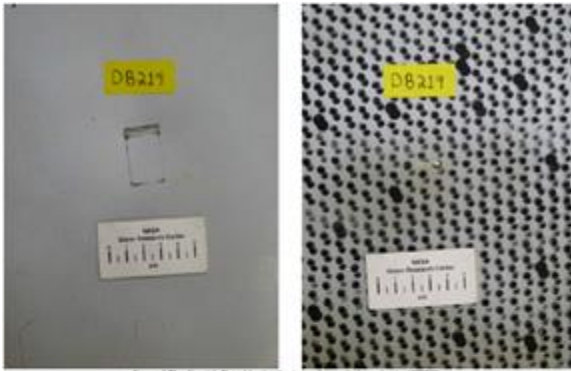
DB219 (146 fps)

DB218 (203 fps)

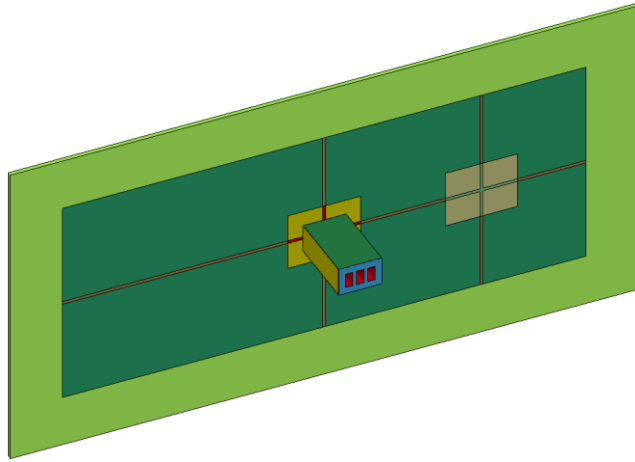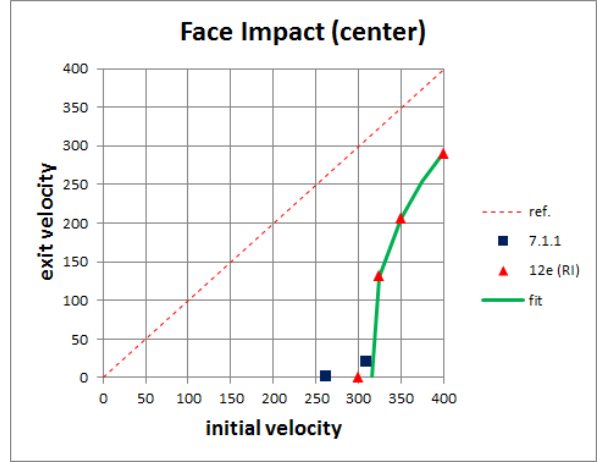(c)
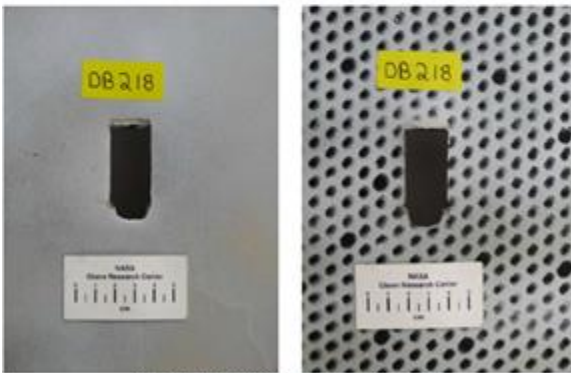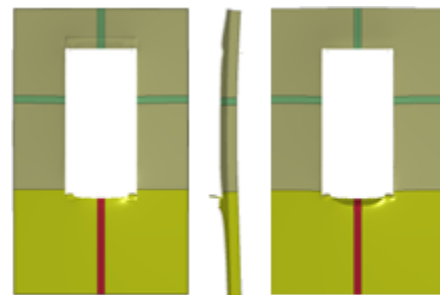
200 fps

(d)

Figure B-6. Simulation results of test setup #6.2.5: (a) impact setup; (b) exit velocities of the projectile; (c) plate deformation in tests [7]; and (d) plate deformation in simulations

(a)

(b)

(c)
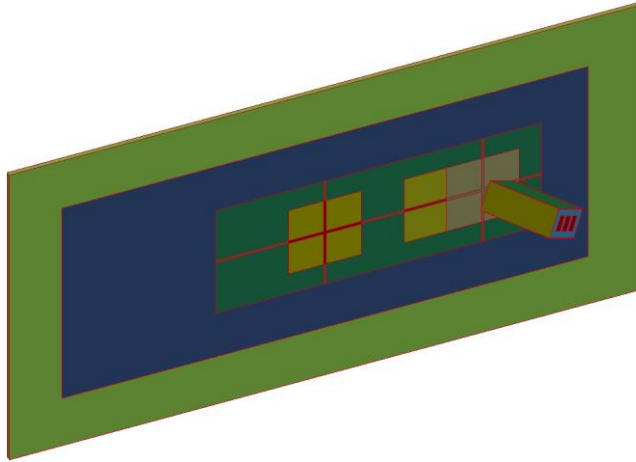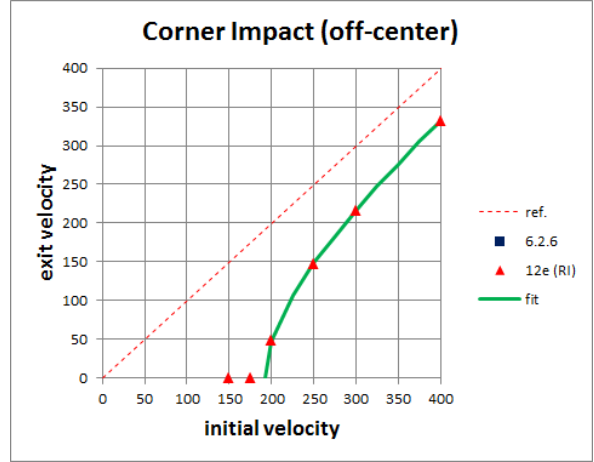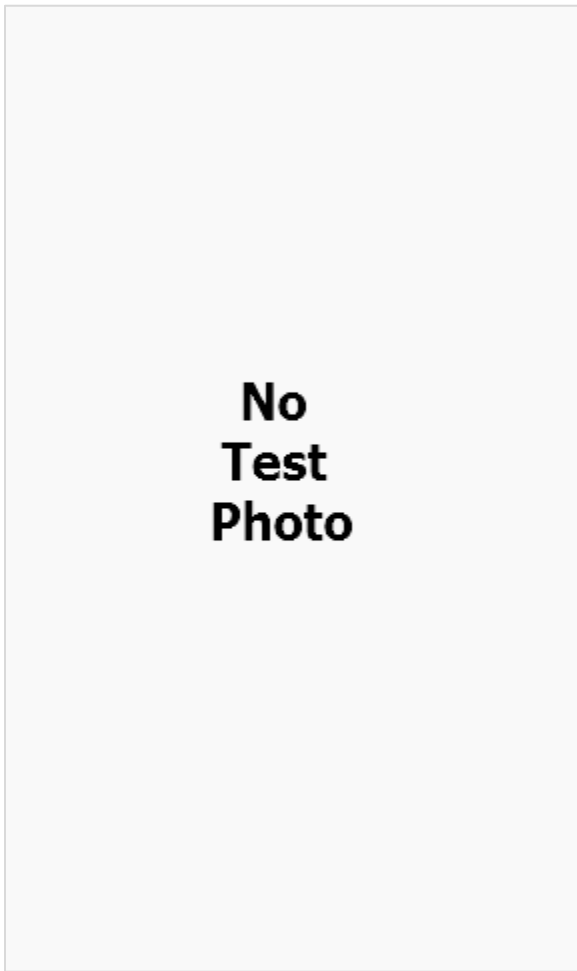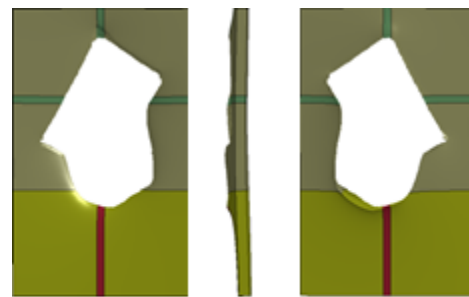
(d)

Figure B-7. Simulation results of test setup #6.2.6: (a) impact setup; (b) exit velocities of the projectile; (c) plate deformation in tests [7]; and (d) plate deformation in simulations
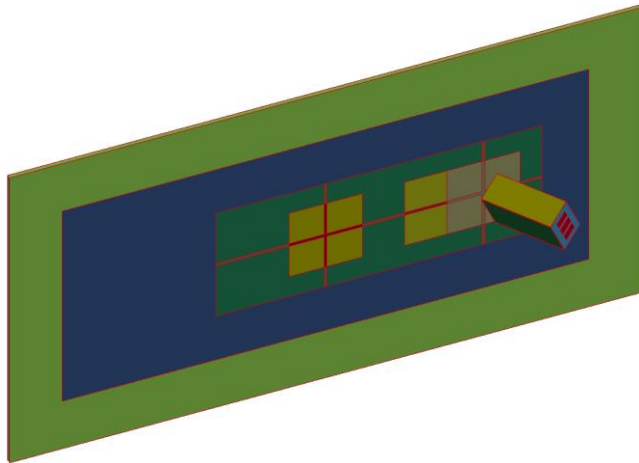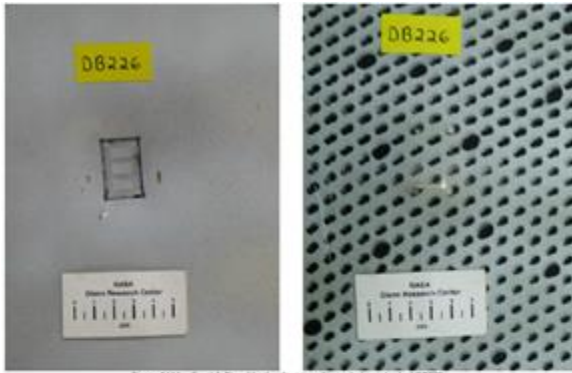
(a)   (b)

DB222 (146 fps)

DB221 (200 fps)
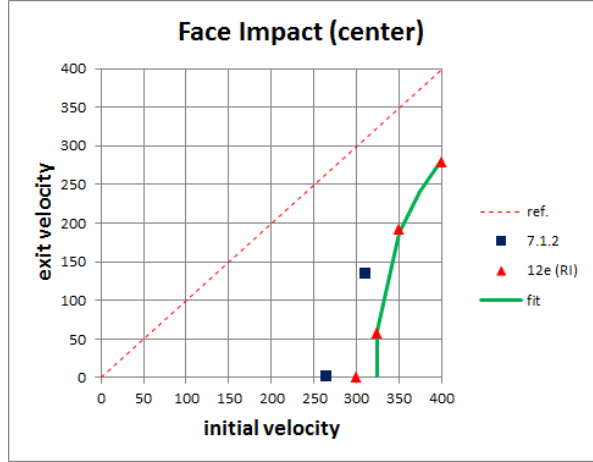

200 fps

(c)   (d)

Figure B-8. Simulation results of test setup #6.2.7: (a) impact setup; (b) exit velocities of the projectile; (c) plate deformation in tests [7]; and (d) plate deformation in simulations
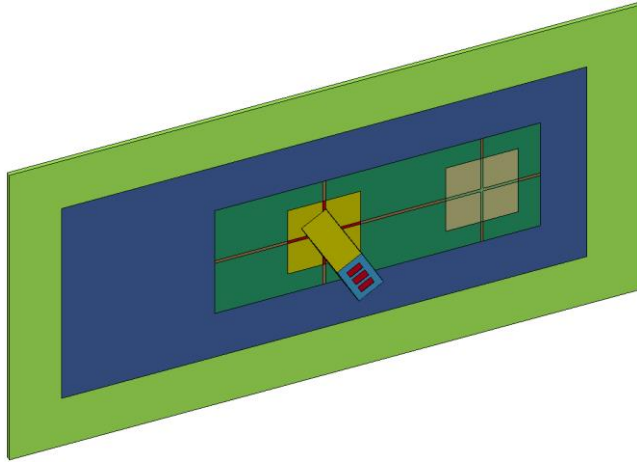
(a)

(b)

DB225 (143 fps)

DB223 (264 fps)

(c)

250 fps

(d)

Figure B-9. Simulation results of test setup #6.2.8: (a) impact setup; (b) exit velocities of the projectile; (c) plate deformation in tests [7]; and (d) plate deformation in simulations
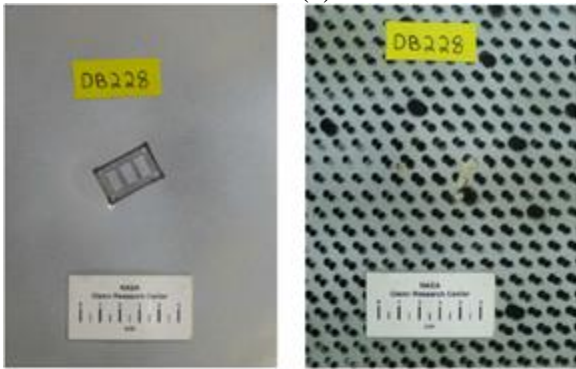
(a)

(b)

DB 226 (263 fps)

DB 227 (310 fps)

(c)

350 fps

(d)

Figure B-10. Simulation results of test setup #7.1.1: (a) impact setup; (b) exit velocities of the projectile; (c) plate deformation in tests [7]; and (d) plate deformation in simulations

(a)

(b)

DB 228 (266 fps)

DB 229 (312 fps)

(c)
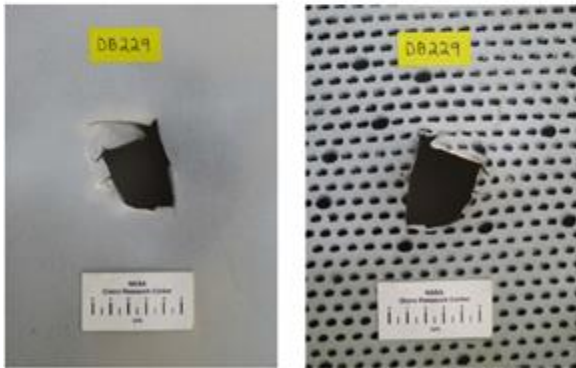
350 fps

(d)

Figure B-11. Simulation results of test setup #7.1.2: (a) impact setup; (b) exit velocities of the projectile; (c) plate deformation in tests [7]; and (d) plate deformation in simulations (Note: the 312 fps shot had a 15º and 14º of both pitch and roll and does not match the simulation case)